RSC Applied Interfaces

ROYAL SOCIETY OF CHEMISTRY

REVIEW

View Article Online
View Journal | View Issue

Check for updates

Cite this: *RSC Appl. Interfaces*, 2025, **2**, 1105

Recent advances in sulfurized polyacrylonitrile cathodes for lithium–sulfur batteries

Ting-Hu Tsai[a] and Yu-Sheng Su *[ab]

Lithium–sulfur (Li–S) batteries are attractive for next-generation energy storage due to the high theoretical capacity (1675 mA h g^{-1}) and energy density (≈2600 Wh kg^{-1}) of sulfur cathodes. However, traditional sulfur cathodes suffer from severe challenges including the electrical insulation of sulfur, large volume changes upon cycling, and the notorious polysulfide shuttle effect that causes rapid capacity fade. In this regard, sulfurized polyacrylonitrile (SPAN) has emerged as a promising cathode material to overcome these issues. By chemically binding sulfur within a carbon–nitrogen polymer matrix, SPAN completely suppresses polysulfide dissolution and shuttle, enabling highly stable cycling. It is synthesized by simple thermal treatment of polyacrylonitrile with sulfur, yielding a covalently bonded S–C network that is compatible with conventional carbonate electrolytes. This review provides a comprehensive overview of SPAN cathodes, including their structural characteristics and unique solid-state redox mechanism, as well as recent advances in material design and performance optimization. We highlight key studies that elucidate the covalent bonding and lithiation chemistry of SPAN, and we survey state-of-the-art strategies from conductive composites and dopants to electrode engineering, which have elevated its electrochemical performance. Finally, remaining challenges and perspectives for practical Li–S batteries with SPAN cathodes are discussed.

Received 1st June 2025,
Accepted 14th July 2025

DOI: 10.1039/d5lf00157a

rsc.li/RSCApplInter

Open Access Article. Published on 15 July 2025. Downloaded on 6/21/2026 12:44:31 AM.
This article is licensed under a Creative Commons Attribution 3.0 Unported Licence.

1. Introduction

Rechargeable Li–S batteries utilize elemental sulfur as the active cathode material. Sulfur offers an extremely high theoretical specific capacity of 1675 mA h g^{-1} (corresponding to the formation of Li_2S) and an energy density up to ~2600 Wh kg^{-1}, far exceeding those of conventional intercalation

[a] *International College of Semiconductor Technology, National Yang Ming Chiao Tung University, 1001 Daxue Road, Hsinchu 30010, Taiwan.*
E-mail: yushengsu@nycu.edu.tw
[b] *Industry Academia Innovation School, National Yang Ming Chiao Tung University, 1001 Daxue Road, Hsinchu 30010, Taiwan*

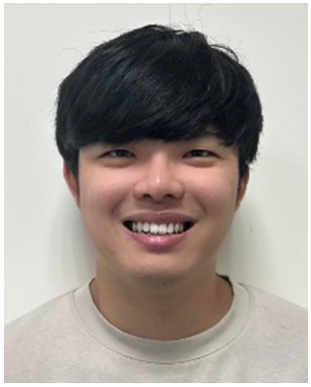

Ting-Hu Tsai

Ting-Hu Tsai received his B.S. degree in Materials Science and Engineering from National Chung Hsing University in 2023. He is currently pursuing his M.S. degree under the supervision of Professor Yu-Sheng Su at the International College of Semiconductor Technology, National Yang Ming Chiao Tung University. His research focuses on polymer-sulfur cathodes and prelithiation strategies for lithium-based batteries. He will join TSMC upon completion of his master's degree.

Yu-Sheng Su

Yu-Sheng Su (Winston) is an Associate Professor at the International College of Semiconductor Technology, National Yang Ming Chiao Tung University (NYCU), Taiwan. He received his Ph.D. in Materials Science and Engineering from The University of Texas at Austin in 2013, and both his B.S. and M.S. degrees from National Tsing Hua University, Taiwan. Dr. Su's research interests include advanced battery technologies, graphene-based materials, and recycling strategies. He has published over 60 journal articles and holds 40 U.S. patents, with total citations exceeding 12 725. He is a recipient of the Yushan Young Fellow Award and 2030 Emerging Young Scholar Award.

© 2025 The Author(s). Published by the Royal Society of Chemistry

Open Access Article. Published on 15 July 2025. Downloaded on 6/21/2026 12:44:31 AM.
This article is licensed under a Creative Commons Attribution 3.0 Unported Licence.

cathodes.[1] These attributes make Li–S systems promising candidates for long-range electric vehicles and grid-scale energy storage.[2] Yet, despite this promise, traditional sulfur cathodes are plagued by fundamental problems that hinder their practical deployment. Key challenges include but are not limited to: electrical insulation, polysulfide dissolution ("shuttle effect"), and volume expansion.[1,3] Elemental sulfur and its fully lithiated product Li_2S are both electronically insulating and have poor Li^+ conductivity.[4] This necessitates the use of conductive additives and limits the active material utilization. During discharge, sulfur is reduced through soluble lithium polysulfide intermediates (Li_2S_n, $4 \leq n \leq 8$).[5,6] These polysulfides readily dissolve into the electrolyte and can diffuse to the lithium anode, causing parasitic reactions and self-discharge.[7] The continuous loss of active sulfur and side-reactions on lithium lead to low coulombic efficiency and rapid capacity fading. The conversion of S to Li_2S entails an ~80% volume expansion in the cathode.[8,9] The repetitive expansion/contraction breaks down the electrode structural integrity and electrical contacts, accelerating performance degradation. Consequently, a conventional sulfur–carbon composite cathode often suffers from limited cycle life and poor rate capability. Extensive research has targeted these issues by impregnating sulfur into porous carbons or polar host materials to trap polysulfides and buffer volume changes.[4,10–14] While such physical confinement strategies (*e.g.*, functional interlayers or modified separators) can mitigate the shuttle effect to an extent, they add complexity and only partially address the intrinsic solubility of sulfur species. There remains a need for a fundamentally different cathode approach that can eliminate polysulfide dissolution at the source. This impetus has driven the development of chemically bound sulfur cathodes, among which sulfurized polyacrylonitrile is one of the most prominent examples.

Sulfurized polyacrylonitrile (often written as SPAN) is an "organic" sulfur cathode wherein sulfur is covalently integrated into a carbon–nitrogen polymer matrix.[15–20] This concept was first realized by Wang *et al.* in the early 2000s, who heated polyacrylonitrile (PAN) with sulfur to create a chemically bonded polymer-sulfur composite.[21,22] In their landmark study, the SPAN material delivered ~850 mA h g^{-1} initial capacity, demonstrating the viability of immobilizing sulfur in a host matrix.[21,22] The key advantage of SPAN lies in its unique "covalent bonding" mechanism that immobilizes sulfur and prevents the generation of free polysulfide anions.[23,24] In contrast to a physical mixture of sulfur in carbon, the sulfur in SPAN is chemically bound to the PAN-derived framework, so upon lithiation it remains anchored and does not dissolve into the electrolyte.[15] This effectively eradicates the polysulfide shuttle problem at its root, enabling Li–S cells with excellent cycle stability.

SPAN is typically synthesized *via* a simple one-step thermal vulcanization of PAN with elemental sulfur. In a representative process, PAN powder is intimately mixed with sulfur and heated (*e.g.* 300–600 °C) under inert atmosphere.[15] During this heat treatment, PAN undergoes partial dehydrogenation and cyclization, reacting with sulfur to form a conjugated carbon–nitrogen backbone with sulfur atoms covalently attached.[23,24] The result is a black, carbon-rich composite in which sulfur is present not as S_8 molecules but as part of the polymeric structure.[23,24] This SPAN material shows better electronic conductivity ($\approx 10^{-4}$ S cm^{-1}) and electrochemical activity, in stark contrast to elemental sulfur ($\approx 10^{-30}$ S cm^{-1}).[25] Furthermore, the sulfur is distributed on a conductive carbonaceous matrix on a molecular scale. This alleviates issues of sulfur agglomeration and large volume changes because the polymeric matrix can buffer mechanical strain and maintain electrical percolation. These features make the SPAN cathode's reaction more controllable, lending itself to high efficiency and longevity. Notably, because no long-chain polysulfides are released during charge/discharge, SPAN electrodes exhibit compatibility with carbonate-based electrolytes.[26] This means that traditional Li–S cells must use ether solvents to stabilize polysulfides; in carbonate electrolytes, soluble polysulfides would react rapidly and foul the cell.[27] SPAN avoids this problem. The ability to use standard Li-ion battery electrolytes and processing techniques is a significant practical merit of SPAN.

This review aims to provide a focused and in-depth overview of SPAN as a cathode material for Li–S batteries, with particular emphasis on its molecular structure, electrochemical redox mechanism, and recent progress in composite cathode design. Rather than surveying the broad Li–S field, this article concentrates on SPAN's unique solid-phase behavior and the strategies that exploit its chemically bonded sulfur framework to overcome the limitations of conventional sulfur cathodes. We begin with a detailed examination of SPAN's molecular architecture and lithium storage mechanism, followed by discussions on composite designs including carbon, graphene, fibrous, and doped SPAN variants. Finally, the review addresses current challenges, electrolyte/binder strategies, and perspectives for practical implementation. This structure is intended to help

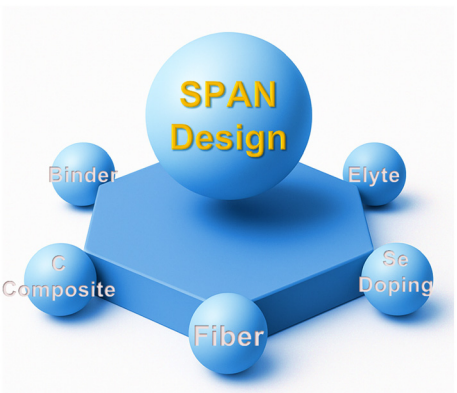

Fig. 1 Conceptual illustration representing the SPAN cathode design strategy. This review covers key approaches including carbon/graphene composites, SPAN fibers, Se-doping, structural engineering, electrolyte optimization, and binder design.

© 2025 The Author(s). Published by the Royal Society of Chemistry

Open Access Article. Published on 15 July 2025. Downloaded on 6/21/2026 12:44:31 AM. This article is licensed under a Creative Commons Attribution 3.0 Unported Licence.

readers gain mechanistic insights while identifying actionable research directions for advancing SPAN-based Li–S batteries (Fig. 1).

2. Molecular structure, bonding characteristics, and formation mechanism of SPAN

2.1 Spectroscopic characterizations of SPAN

SPAN is an advanced cathode material that demonstrates significant advantages over conventional sulfur cathodes due to its unique molecular structure and electrochemical characteristics. The detailed molecular configuration of SPAN has been extensively investigated using multiple advanced characterization techniques including Fourier-transform infrared spectroscopy (FT-IR), Raman spectroscopy, solid-state NMR, X-ray photoelectron spectroscopy (XPS), X-ray diffraction (XRD), and theoretical density functional theory (DFT) calculations.

FT-IR spectra analysis of SPAN (Fig. 2a) reveals characteristic peaks at 1200–1600 cm^{-1} and 803 cm^{-1} corresponding to the formation of six-membered rings containing conjugated C═C and C═N bonds.[28] Peaks at 515, 670, and 941 cm^{-1} further indicate the presence of S–S stretching, C–S stretching, and ring-breathing modes of side-chain S–S bonds, confirming successful sulfurization.[28,29] Complementary Raman spectroscopy (Fig. 2b) further confirms these observations, identifying peaks at 460 and 530 cm^{-1} as characteristic of S–S bonds, while peaks at 805 and 930 cm^{-1} correspond to C–S stretching and six-membered ring stretches involving S–S bonds, respectively.[28] Additional Raman signals at 1566 and 1360 cm^{-1} (G-band and D-band) imply graphitic and disordered carbon structures within SPAN.[28,30]

Solid-state ^{13}C NMR analysis (Fig. 2c) provides deeper insights into the molecular framework, identifying distinct peaks at approximately 122 ppm (C═C) and 153 ppm (C═N), as well as a new resonance at 165 ppm attributed to the C–S bonds formed during sulfurization.[28–30] Computational DFT simulations further validated these assignments, suggesting that SPAN's active structure consists predominantly of cyclic units interconnected *via* sulfur atoms (structure I, shown in Fig. 2d), supporting a repeating or periodic unit ($C_3N_1S_1$) within its structure.[31] Elemental analysis aligns closely with this molecular model, indicating approximately 39 wt% sulfur content, closely matching theoretical predictions.[31,33]

XPS characterization (Fig. 2e) also supports this molecular structure, demonstrating high-resolution S 2p spectra that identify distinct peaks attributed to C–S bonds and S–S bonds, indicating short-chain organosulfides and amorphous sulfur phases within SPAN.[28] These findings are consistent with the

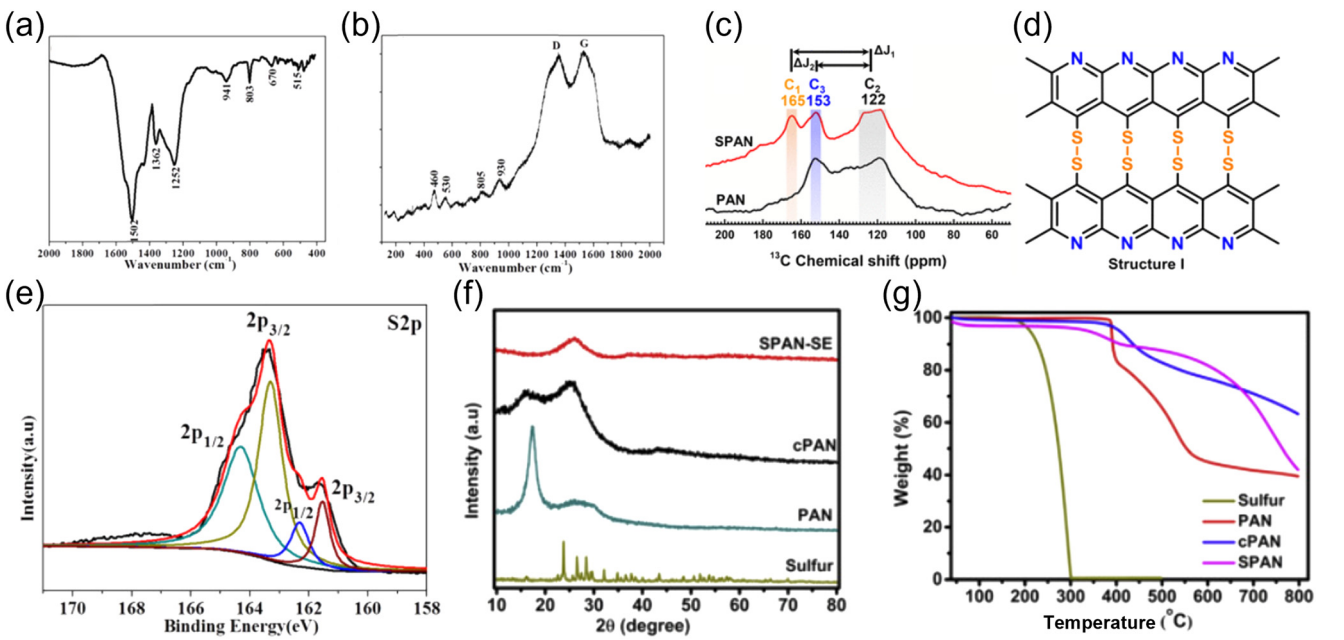

Fig. 2 Comprehensive structural and electrochemical characterization of SPAN. (a) FT-IR spectra show characteristic signals from C═C and C═N bonds, along with vibrational modes associated with S–S and C–S bonds, confirming successful sulfurization. (b) Raman spectra reveal S–S and C–S bond vibrations, six-membered ring breathing modes, and D/G bands indicative of graphitic and disordered carbon structures. Reproduced with permission from ref. 28. Copyright 2018, Elsevier. (c) Solid-state ^{13}C NMR identifies key carbon environments including unsaturated and heteroatom-linked carbon species formed during sulfurization. (d) DFT simulations support a cyclic molecular model featuring sulfur-bridged repeating units. Reproduced with permission from ref. 31. Copyright 2018, American Chemical Society. (e) XPS S 2p spectra indicate the coexistence of C–S and S–S bonds, suggesting the presence of short-chain organosulfides and amorphous sulfur. Reproduced with permission from ref. 28. Copyright 2018, Elsevier. (f) XRD patterns confirm an amorphous structure induced by thermal sulfurization and polymer cyclization. (g) TGA confirms enhanced thermal stability and strong covalent bonding of sulfur in the polymer matrix. Reproduced with permission from ref. 34. Copyright 2020, Elsevier.

Open Access Article. Published on 15 July 2025. Downloaded on 6/21/2026 12:44:31 AM.
This article is licensed under a Creative Commons Attribution 3.0 Unported Licence.

molecular structural model derived from FTIR, Raman, and NMR analyses.[28] XRD patterns of SPAN synthesized at varying temperatures confirm that the sulfurization process at 350 °C leads to a fully amorphous structure, evidenced by broad diffraction peaks at $2\theta = 26.5°$ (Fig. 2f), corresponding to cyclic structures formed through cyclization and dehydrogenation processes.[30,34] Thermal gravimetric analysis (TGA) (Fig. 2g) and elemental analysis further confirm that covalently bonded sulfur sublimates at higher temperatures compared to elemental sulfur, reinforcing the formation of strong C–S and S–S bonds within the polymer matrix.[34]

2.2 Effects of synthesis temperature on SPAN structure

The synthesis temperature critically governs the chemical structure and electrochemical performance of SPAN materials. At temperatures below 150 °C, sulfur and PAN do not chemically interact, resulting in physical mixtures with poor electrochemical activity.[35] Between 200–250 °C, sulfur accelerates PAN cyclization but does not form covalent bonds.[35] True chemical bonding, such as C–S and S–S linkages, emerges only above 300 °C (Fig. 3a), accompanied by the formation of thioamide structures and conjugated aromatic backbones.[35] These features enhance electronic conductivity and lithium storage capability. Studies show that a synthesis temperature above 350 °C yields optimal structural integrity, high sulfur utilization, and stable cycling performance.[35,36] In contrast, excessively high temperatures (>600 °C) lead to over-carbonization and denitrogenation (Fig. 3b), significantly reducing sulfur content and reversibility.[36] Therefore, a carefully controlled synthesis temperature (typically 300 to 500 °C) is essential to balance covalent sulfur incorporation with backbone conductivity, ensuring high-performance SPAN cathodes.

2.3 Influence of sulfur content of SPAN on electrochemical behavior

The sulfur content in SPAN plays a critical role in determining its electrochemical performance and structural stability. While the initial PAN/sulfur mass ratio influences the potential sulfur loading, other synthesis parameters such as temperature, gas flow rate, and heating duration also

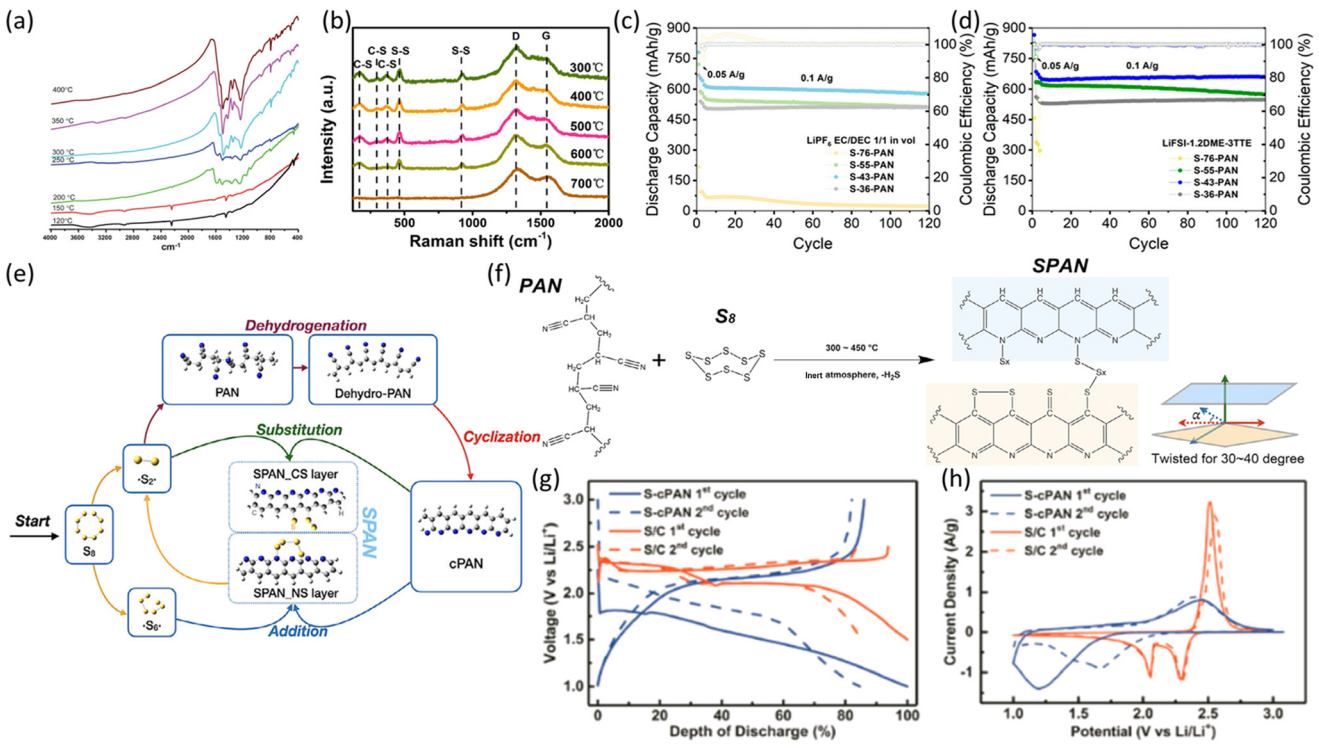

Fig. 3 (a) FTIR spectra of SPAN-based materials synthesized at different temperatures, showing the evolution of characteristic functional groups. Reproduced with permission from ref. 35. Copyright 2012, Royal Society of Chemistry. (b) Raman spectra of SPAN/CNT composites prepared at 300–700 °C, illustrating the development of C–S and S–S bonding and graphitic features. Reproduced with permission from ref. 36. Copyright 2021, Elsevier. (c and d) Discharge capacity and coulombic efficiency of SPAN half-cells cycled in (c) carbonate-based and (d) ether-based electrolytes, demonstrating electrolyte-dependent performance. Reproduced with permission from ref. 37. Copyright 2023, American Chemical Society. (e) Schematic overview of the SPAN synthesis mechanism, highlighting key steps including sulfur radical formation, PAN dehydrogenation and cyclization, and covalent sulfur incorporation. (f) Molecular structure model of SPAN synthesized from PAN and S_8, where S_x species (x = 1–6) bond to carbon or nitrogen atoms within or between polymer chains. Reproduced with permission from ref. 38. Copyright 2025, Wiley-VCH. (g) GCD profiles demonstrate activation behavior and a solid-phase lithiation mechanism with broad voltage profiles. (h) CV curves reveal initial irreversible reduction followed by stabilized redox behavior, consistent with conjugated bond interactions and nitrogen-assisted lithiation. Reproduced with permission from ref. 39. Copyright 2021, Elsevier.

© 2025 The Author(s). Published by the Royal Society of Chemistry

Open Access Article. Published on 15 July 2025. Downloaded on 6/21/2026 12:44:31 AM. This article is licensed under a Creative Commons Attribution 3.0 Unported Licence.

significantly affect the final sulfur content and chemical bonding state. For instance, three SPAN samples synthesized with different sulfur contents (46.3, 42.0, and 33.7 wt%) exhibited distinct electrochemical behaviors.[40] The sample with 42.0 wt% sulfur delivered the best balance of initial capacity (~895.6 mA h g^{-1}), coulombic efficiency, and cycle retention (~97.2%), suggesting an optimal sulfur range around 40–43 wt%.[40] In contrast, the 46.3 wt% sulfur sample showed higher capacity but poorer reversibility, attributed to the presence of unbound elemental sulfur.[40] Another complementary study demonstrated that controlling the synthesis temperature from 250 to 450 °C adjusted sulfur content from 76% down to 36%, and that SPAN synthesized at 300 °C (S-43-PAN) retained covalently bound sulfur without excess elemental phases, leading to superior performance in both carbonate and ether-based electrolytes (Fig. 3c and d).[37] These results collectively highlight that excessive sulfur loading may result in free sulfur or unstable S–S bonds, while insufficient sulfur reduces capacity. Therefore, achieving an optimal sulfur content, typically in the 40–45 wt% range, through well-controlled synthesis conditions is essential for designing high-performance SPAN cathodes.[37,40,41]

2.4 SPAN formation mechanism and multilayered molecular configuration

The formation of SPAN is governed by a complex thermally driven mechanism involving sulfur radical generation, PAN backbone transformation, and covalent sulfur incorporation. Recent theoretical and experimental investigations have elucidated the detailed reaction pathways and molecular configurations of SPAN (Fig. 3e).[38] The process initiates with the thermal cracking of elemental S_8 into diradical fragments such as $\cdot S_2\cdot$ and $\cdot S_6\cdot$, which promote PAN dehydrogenation and intramolecular cyclization.[38] These transformations lead to the formation of conjugated cPAN frameworks.[38] Upon further heating, the reactive sulfur species bond with both carbon and nitrogen sites on cPAN, forming covalent C–S and N–S linkages. These reactions are kinetically favored around 300–500 °C, consistent with experimental conditions yielding optimal electrochemical performance.[38]

The resulting SPAN material exhibits a unique multilayered structure comprising alternating C–S and N–S planes twisted at ~30–40° (Fig. 3f), interconnected by S_x bridges (C–S_x–N).[38] This configuration enhances structural rigidity and chemically confines sulfur, suppressing polysulfide formation. The maximum chemically bonded sulfur content is estimated at ~63.5 wt%, correlating to a theoretical capacity of >1000 mA h g^{-1}, although practical values are typically lower due to synthesis constraints.[38]

3. Electrochemical behavior and lithium storage mechanism

The electrochemical performance of SPAN in lithium–sulfur batteries exhibits distinctive features, notably a significant initial voltage hysteresis and irreversible capacity loss attributed primarily to poor initial interfacial electrical contact between SPAN grains and conductive additives, and irreversible reduction of short, low-delocalized conjugated carbon bonds within SPAN fragments.[17] These initial issues diminish substantially upon subsequent cycles due to improved electrical contact and increased conjugation within the polymer backbone.[17] Unlike conventional sulfur–carbon cathodes that exhibit dual voltage plateaus associated with solid–liquid–solid transitions,[1,4–6] SPAN electrodes demonstrate a single, broad voltage plateau, indicative of a solid-to-solid single-phase lithiation/delithiation mechanism.[17,39] This mechanism effectively eliminates the dissolution of lithium polysulfides into electrolyte solutions, significantly enhancing the cycle stability and mitigating the self-discharge phenomena commonly observed in traditional Li–S systems.[17,39]

Electrochemical characterizations, including galvanostatic charge/discharge (GCD) profiles and cyclic voltammetry (CV), as displayed in Fig. 3g and h, illustrate that during initial cycling, SPAN undergoes activation processes involving cleavage of S–S bonds, forming radical intermediates that facilitate reversible lithium-ion interactions.[39] Specifically, conjugated double bonds (C=C and C=N) in the polymer backbone react with lithium ions to form stable Li–C–C–Li and Li–C–N–Li structures, contributing additional reversible capacities beyond the theoretical capacity of elemental sulfur.[28] Although some lithium remains irreversibly trapped during initial cycling, this residual lithium enhances conductivity and reduces electrode polarization, improving subsequent cycling stability and discharge voltage profiles.[17,28]

An early study indicates that the sulfur moieties in SPAN (often considered to be S_2 or S_3 units attached to the carbon matrix) are reduced to form lower sulfide species and ultimately Li_2S, without releasing long polysulfide chains into the electrolyte.[30] For example, one report suggested that sulfur in SPAN is predominantly present as S_2 or S_3 units, which directly convert to Li_2S_2 and Li_2S_3 during discharge.[30] These short-chain sulfur fragments are strongly bound within the polymer network, suppressing dissolution and enabling a quasi-solid-state redox pathway. This further supports the observed absence of long-lived polysulfide intermediates and aligns with SPAN's compatibility with carbonate-based electrolytes.

Recent studies further reveal that the lithiation of SPAN does not involve free polysulfides but proceeds *via* a solid–solid mechanism where Li_2S nucleates directly at the nitrogen-rich polymer backbone.[42,43] DFT simulations suggest that covalently bonded oligo(sulfide) chains undergo stepwise cleavage, forming Li_2S that remains anchored or interacts strongly with the SPAN matrix, enhancing reversibility and suppressing polysulfide dissolution.[42,43] SEM observations confirm uniform Li_2S nanoflake formation and decomposition on SPAN fibers during cycling,[44] while recent work shows that Li_2S can also be chemically reactivated *via* Li_2S_8-mediated redox pathways during charging.[45] To summarize, these results indicate that SPAN

Open Access Article. Published on 15 July 2025. Downloaded on 6/21/2026 12:44:31 AM. This article is licensed under a Creative Commons Attribution 3.0 Unported Licence.

enables localized, reversible Li_2S formation without soluble intermediates, offering a stable lithiation mechanism distinct from traditional sulfur cathodes.

In situ spectroscopic analyses combined with DFT calculations have elucidated the critical role of nitrogen doping within the polymer structure, identifying stable N–S and partial C–S bonds that significantly contribute to the solid-phase redox processes.[34,39] The unique N–S_x–N configurations within SPAN further reinforce its electrochemical stability and high rate capability, positioning nitrogen doping as a crucial factor in optimizing cathode performance.[39]

In short, comprehensive characterization has conclusively established that SPAN's molecular architecture consists of short sulfur chains covalently bonded to cyclized, partially dehydrogenated polyacrylonitrile backbones, enriched with conjugated C═N and C═C bonds. This structural configuration underpins its robust electrochemical performance, characterized by solid-state lithium storage mechanisms free from polysulfide dissolution.

4. Modified and ternary SPAN composite cathodes

To address the intrinsic limitations of pristine SPAN, a wide range of modification strategies have been explored. In this section, we focus on representative and widely studied approaches that integrate carbonaceous materials, graphene, fiber-based morphologies, and heteroatom dopants (*e.g.*, selenium) into SPAN-based cathodes. These strategies were selected due to their strong mechanistic relevance, frequent appearance in numerous publications, and demonstrated ability to enhance key electrochemical properties such as interfacial conductivity, structural integrity, sulfur utilization, and compatibility with practical cell configurations. While many other modification routes have been reported, we emphasize those that exhibit clear and consistent benefits under various testing conditions. We begin by summarizing carbon-based SPAN composites, ranging from simple blends to more complex hierarchical architectures, and then discuss fiber-integrated designs, selenium-doped systems, and architecturally engineered morphologies that further improve SPAN cathode performance.

4.1 Carbon-engineered SPAN composites

Microporous carbon particles (MCPs) encapsulated within PAN nanofibers (S/MCPs-PAN nanofibers) leverage the advantages of sulfur-loaded MCPs and structural PAN nanofibers fabricated by electrospinning (Fig. 4a and b).[46] This structure provides ample sulfur loading and stable cycling, exhibiting a reversible capacity of 789.7 mA h g^{-1} (composite) with 84.4% retention after 200 cycles (Fig. 4c).[46] Ionic and electronic transport channels from PAN fibers enhance electrochemical activity and sulfur utilization. SPAN composites with activated conductive carbon black (A-CCB) employ dual-mode sulfur fixation (microstructure shown in Fig. 4d), including chemical bonding to partially carbonized PAN (cPAN) and physical loading onto A-CCB.[47] Furthermore, high-concentration lithium salts (LiTFSI) and viscous solvents significantly enhance cycle stability by suppressing polysulfide dissolution.[47] Optimal sulfur loading (56 wt%) in concentrated electrolyte achieves balanced capacity (578.1 mA h g^{-1} composite after 100 cycles) and stability (Fig. 4e).[47] Another report demonstrated that SPAN embedded within a porous carbon matrix can enhance lithium storage and cycle stability (Fig. 4f).[48] The porous carbon in PAN-S/C composite improves electronic conductivity and structural integrity, achieving a reversible discharge capacity of 658.8 mA h g^{-1}, with 95% retention after 50 cycles, surpassing the mechanically mixed PAN-S/C mixture sample, as compared in Fig. 4g.[48]

Carbon-coated SPAN (C@S/PAN) composites use a protective carbon coating to improve sulfur utilization and mitigate electrode volume changes (microstructures shown in Fig. 4h).[49] The core–shell architecture reduces electrochemical polarization, providing an initial capacity of 1416 mA h g^{-1} with ~89% retention after 200 cycles and excellent rate capability (Fig. 4i).[49] Moreover, integrating multi-wall carbon nanotubes (MWCNTs) with SPAN composites provides robust 1D electron transport channels and structural stability (Fig. 4j).[4,38–41,53] SPAN/MWCNT composites demonstrate superior cycling and rate performance, maintaining high capacities (~630 mA h g^{-1} after 200 cycles at 0.2C) and effectively managing volume changes.[50]

4.2 Graphene-engineered SPAN architectures

PAN nanoparticles anchored on graphene nanosheets (GNS) derived from graphene oxide (Fig. 5a) significantly enhance sulfur dispersion, cycling stability, and rate performance.[54] The conductive GNS scaffold improves sulfur utilization, delivering reversible capacities around 1500 mA h g^{-1} (sulfur basis) with ~80% retention after 100 cycles (Fig. 5b), outperforming the bare SPAN cathode (pPAN-S).[54] Another similar study, combining SPAN with reduced graphene oxide (RGO) using a different order of processing exhibited in Fig. 5c also yields composites with enhanced electrical conductivity and structural integrity.[10,55,56] The RGO network reduces electrode polarization, delivering high reversible capacities (1467 mA h g^{-1}) and about 85% retention after 100 cycles, improving rate capability and cycle performance (Fig. 5d).[55] Hierarchically structured composites combining PAN, kombucha-derived porous carbon, and graphene oxide (S/PAN/KC/GO) achieve superior sulfur dispersion and ionic/electronic transport (Fig. 5e).[57] The composite retains 1193 mA h g^{-1} after 100 cycles, demonstrating excellent polysulfide adsorption, shuttle suppression, and enhanced rate performance due to its hierarchical pore structure.[57]

3D holey graphene/SPAN composites feature covalently bonded sulfur within porous graphene aerogels (Fig. 5f), significantly mitigating polysulfide shuttling and supporting high mass loading (15.2 mg cm^{-2}).[58] This composite exhibits

© 2025 The Author(s). Published by the Royal Society of Chemistry

Open Access Article. Published on 15 July 2025. Downloaded on 6/21/2026 12:44:31 AM.
This article is licensed under a Creative Commons Attribution 3.0 Unported Licence.

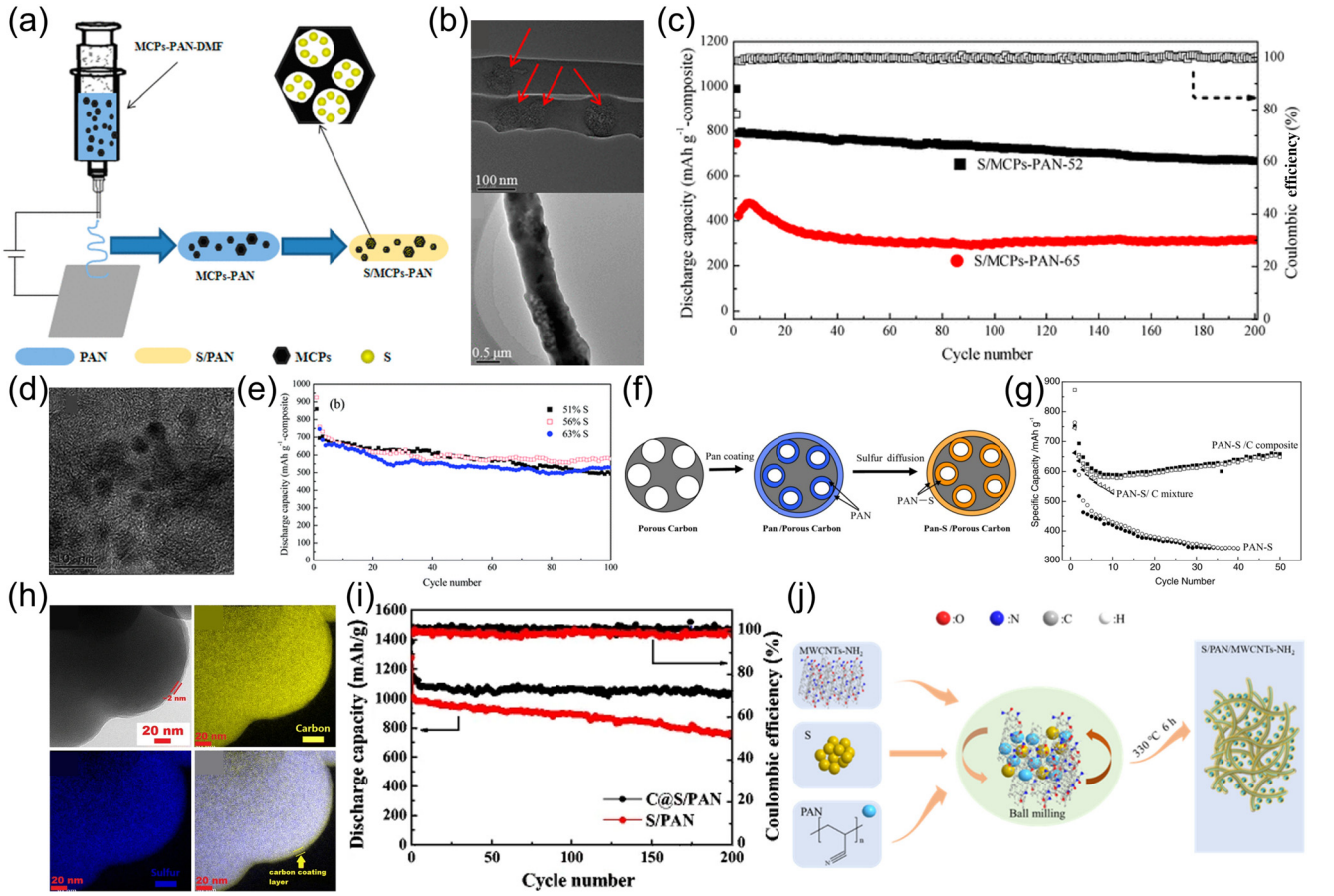

Fig. 4 Carbon/SPAN composite cathode designs for enhanced electrochemical performance. (a and b) Schematic and micrograph images of S/MCPs-PAN nanofibers combining microporous carbon particles and electrospun PAN fibers. (c) Cycling performance shows high capacity retention due to improved ionic/electronic transport. Reproduced with permission from ref. 46. Copyright 2017, American Chemical Society. (d) SPAN/A-CCB composite utilizes dual-mode sulfur fixation *via* chemical and physical confinement. (e) Enhanced stability in concentrated electrolyte with optimized sulfur loading. Reproduced with permission from ref. 47. Copyright 2014, Royal Society of Chemistry. (f) Porous carbon-embedded SPAN composite exhibits improved conductivity and structure. (g) Comparative cycling performance highlights the advantage of structural integration over physical mixing. Reproduced with permission from ref. 48. Copyright 2013, IOP Publishing. (h) Microstructure of carbon-coated SPAN (C@S/PAN) composites featuring a core–shell architecture that mitigates volume changes and enhances sulfur utilization. (i) Electrochemical performance showing reduced polarization, high capacity retention, and excellent rate capability. Reproduced with permission from ref. 49. Copyright 2017, Springer Nature. (j) Schematic of SPAN/MWCNT composite structure, where integrated MWCNTs offer efficient electron transport and structural robustness, supporting long-term cycling stability. Reproduced with permission from ref. 50. Copyright 2023, American Chemical Society.

exceptional cycling stability (81.5% capacity retention after 1500 cycles), superior electron conductivity, and fast lithium-ion transport, ideal for high-rate applications (Fig. 5g).[58] The interconnected nanopores within the 3D holey graphene enable rapid electrolyte penetration and ion transport, which is critical for maintaining high capacity under both fast charge/discharge rates and thick electrode conditions. Additionally, 2D-SPAN/graphene composites, formed by high-pressure pelletization (Fig. 5h), integrate graphene nanosheets to enhance conductivity, structural stability, and minimize lithium polysulfide dissolution.[59] The compact 2D geometry facilitates rapid electrochemical reactions, delivering unprecedented areal capacities (11 mA h cm^{-2} at 10 mg cm^{-2} loading, Fig. 5i) and outstanding cycling stability over 300 cycles, demonstrating strong potential for practical, high-performance Li–S batteries.[59] Notably, a pouch-type Li–S battery employing a 2D-SPAN/graphene cathode and modified electrolyte has been reported to achieve an areal capacity of 6 mA h cm^{-2} and stable cycling over 150 cycles at 0.5C (Fig. 5j), further supporting its scalability.[59]

These carbon and graphene/SPAN composite strategies collectively highlight that carefully engineered carbon-based architectures significantly enhance conductivity, cycling stability, sulfur utilization, and overall electrochemical performance, providing practical, scalable solutions for advanced Li–S battery systems.

4.3 Fiber-based SPAN composites

Fiber-based SPAN cathodes offer advantages of enhanced structural stability, improved ion and electron transport, and high active material utilization in Li–S batteries. Various

Open Access Article. Published on 15 July 2025. Downloaded on 6/21/2026 12:44:31 AM.
This article is licensed under a Creative Commons Attribution 3.0 Unported Licence.

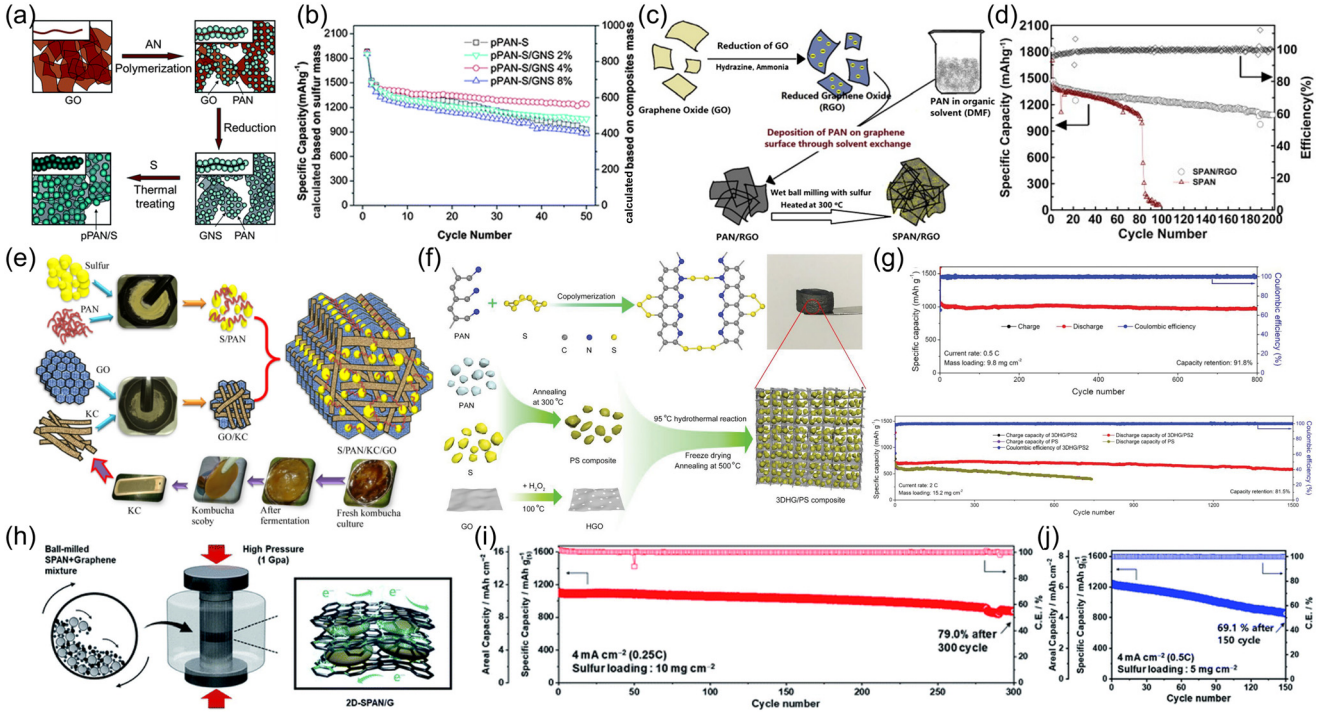

Fig. 5 Graphene-engineered SPAN cathode architectures for Li–S batteries. (a and b) PAN nanoparticles anchored on GNS enhance sulfur dispersion and cycling stability. Reproduced with permission from ref. 54. Copyright 2012, Royal Society of Chemistry. (c and d) SPAN/RGO composites improve conductivity and capacity retention. Reproduced with permission from ref. 55. Copyright 2014, Elsevier. (e) Hierarchical SPAN/KC/GO structure enables effective ion/electron transport. Reproduced with permission from ref. 57. Copyright 2020, Springer Nature. (f and g) 3D holey graphene/SPAN composites suppress shuttling and support high mass loading with long cycle life. Reproduced with permission from ref. 58. Copyright 2021, Wiley-VCH. (h and i) 2D-SPAN/graphene pellets enable high areal capacity and robust cycling. (j) Pouch-type full cell with 2D-SPAN/graphene cathode demonstrates scalability. Reproduced with permission from ref. 59. Copyright 2022, Royal Society of Chemistry.

strategies have been explored, progressively integrating complex structures to optimize electrochemical performance. Simple electrospun SPAN fibers demonstrated improved redox kinetics and high reversible capacities due to the inherent fiber morphology promoting efficient ion/electron transport and reduced volume expansion.[60] Hollow tubular SPAN fibers further significantly enhanced redox reversibility and capacity retention (up to 1236 mA h g^{-1} after 300 cycles) by mitigating the shuttle effect intrinsic to SPAN cathodes (Fig. 6a–c).[61] In addition, introducing conductive additives such as vapor-grown carbon fibers (VGCF) into SPAN composites (SVF composite) enhanced conductivity (Fig. 6d and e), resulting in superior rate capabilities (903 mA h g^{-1} after 150 cycles at 1C and 600 mA h g^{-1} at 2C over 300 cycles shown in Fig. 6f and g, respectively).[62] The interconnected porous structure facilitated electrolyte penetration and rapid ion diffusion, maintaining structural integrity even under high current densities.[62,63] A scalable fibrous SPAN was also prepared by sulfurizing commercial PMMA/PAN textile fibers, yielding up to 46 wt% covalently bound sulfur and a porous morphology that enabled superior rate capability (up to 8C) and >1000-cycle stability, outperforming particulate SPAN.[64] Moreover, graphene integration into SPAN fibers (SFPAN-*g*-rGO; Fig. 6h) achieved an ultrahigh sulfur content (~53 wt%) and significantly improved cycling stability (capacity retention of 96.8% after 200 cycles at 0.2C; Fig. 6i).[65] The graphene incorporation enhanced electron conductivity and mechanical robustness, supporting rapid reaction kinetics and prolonged cycle life.[65]

Catalytic metal sulfides integrated with SPAN fibers provided dual-active cathode materials exhibiting synergistic interactions. FeS nanoparticles promoted polysulfide adsorption and catalytic oxidation of Li_2S (Fig. 6j), substantially improving cycling stability (688.6 mA h g^{-1} retained after 500 cycles at 1 A g^{-1}; (Fig. 6k)) and energy density (over 900 Wh kg^{-1}), outperforming commercial cathodes like $LiCoO_2$.[66] Composites such as CoS_2-SPAN-CNT further exhibited exceptional electrical conductivity and high sulfur loading capabilities (Fig. 6l and m), reaching remarkable areal capacities (8.1 mA h cm^{-2} at 5.9 mg cm^{-2} sulfur loading) suitable for flexible, high-energy-density applications.[67] Advanced nanostructured composites like FeMn@GN-SPAN significantly accelerated lithium polysulfide redox reactions and improved cycle stability, retaining 845 mA h g^{-1} over 500 cycles due to the catalytic effect of graphene nanosheets and $Fe_xMn_{1-x}S$ nanoparticles within SPAN fibers (Fig. 6n).[68]

Optimizing synthesis conditions, such as controlled sulfurization temperature, further enhances electrochemical performance. For instance, SPAN/CNT fibers synthesized at 500 °C (SPAN/CNT-500) achieve a high reversible capacity of 1280 mA h g^{-1} after 200 cycles at 400 mA g^{-1} with minimal degradation, owing to optimal sulfur bonding, uniform

© 2025 The Author(s). Published by the Royal Society of Chemistry

Open Access Article. Published on 15 July 2025. Downloaded on 6/21/2026 12:44:31 AM.
This article is licensed under a Creative Commons Attribution 3.0 Unported Licence.

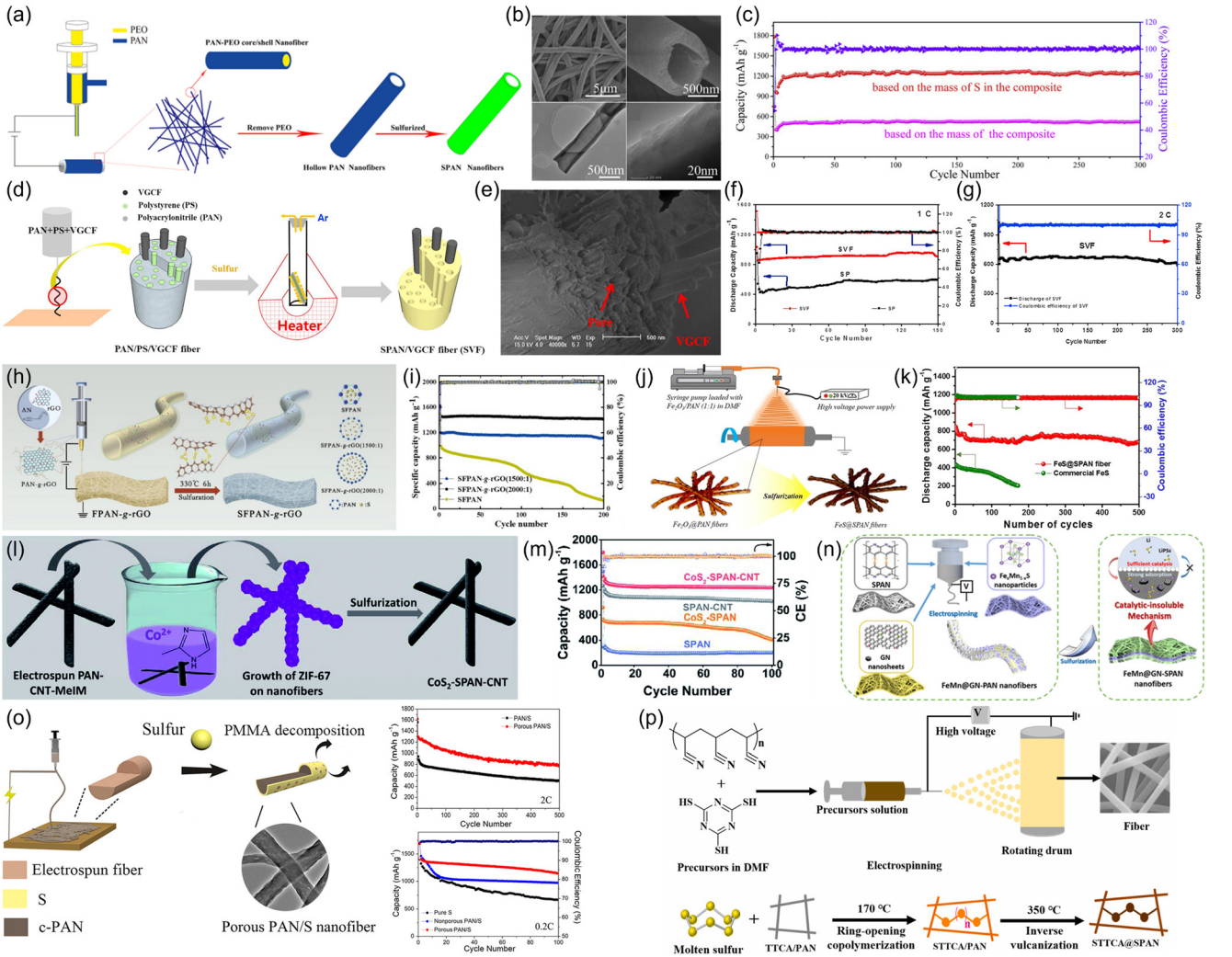

Fig. 6 Structural evolution and electrochemical performance of fiber-based SPAN cathodes. (a–c) Hollow tubular fibers mitigate shuttle effects, enhancing capacity retention. Reproduced with permission from ref. 61. Copyright 2020, Elsevier. (d–g) Conductive additives like VGCF improve rate capability and cycling stability of SPAN fibers. Reproduced with permission from ref. 62. Copyright 2019, Elsevier. (h and i) Graphene-enhanced SPAN fibers enable high sulfur loading and robust cycling. Reproduced with permission from ref. 65. Copyright 2023, Elsevier. (j and k) Catalytic FeS integration boosts redox kinetics and long-term stability. Reproduced with permission from ref. 66. Copyright 2019, American Chemical Society. (l) Structure of CoS_2-SPAN-CNT composite enabling enhanced conductivity and sulfur utilization. (m) High areal capacity achieved by CoS_2-SPAN-CNT cathode. Reproduced with permission from ref. 67. Copyright 2020, Royal Society of Chemistry. (n) FeMn@GN-SPAN delivers high capacity and long cycle life *via* catalytic redox acceleration. Reproduced with permission from ref. 68. Copyright 2021, American Chemical Society. (o) Porous SPAN nanofiber structures promote efficient ion/electron transport. Reproduced with permission from ref. 63. Copyright 2021, Elsevier. (p) STTCA@SPAN demonstrates strong polysulfide confinement and compatibility with carbonate electrolytes. Reproduced with permission from ref. 69. Copyright 2022, Elsevier.

dispersion, and improved conductivity.[70] Innovative porous SPAN fiber structures, synthesized with pore-forming agents like PMMA (Fig. 6o), exhibited improved ion/electron diffusion pathways, resulting in superior cycling stability (1144 mA h g^{-1} at 0.2C after 100 cycles and 794 mA h g^{-1} at 2C after 500 cycles).[63] Novel SPAN fiber structures using trithiocyanuric acid (STTCA@SPAN) shown in Fig. 6p demonstrated chemically bonded short-chain sulfur species, high sulfur content (58 wt%), and exceptional compatibility with carbonate electrolytes.[69] This led to high initial capacities (1301 mA h g^{-1}), excellent cycle stability (982 mA h g^{-1} after 400 cycles at 0.1C), and notable high-rate performance.[69]

In summary, evolving SPAN fiber cathode designs have progressively integrated structural sophistication, conductive frameworks, catalytic components, doping strategies, and optimized synthesis methods, demonstrating significant improvements in electrochemical performance, rate capability, and cycling stability.

4.4 Selenium-doped SPAN composites

Introducing selenium into SPAN composites can significantly enhance their electrochemical performance, addressing intrinsic limitations of traditional SPAN materials, such as

Open Access Article. Published on 15 July 2025. Downloaded on 6/21/2026 12:44:31 AM.
This article is licensed under a Creative Commons Attribution 3.0 Unported Licence.

low sulfur content and sluggish kinetics.[60] Various selenium doping strategies have been reported, each leveraging unique electrochemical mechanisms to optimize battery performance. In simple Se-doped SPAN systems (SeSPAN), selenium atoms serve as additional binding sites for sulfur species, facilitating increased sulfur loading (~60 wt%) compared to conventional SPAN (<50 wt%). This results from reversible Se–S bonds that complement existing C–S interactions, stabilizing sulfur species and preventing dissolution. Moreover, the enhanced electronic conductivity from selenium doping notably improves the redox kinetics, leading to reduced electrochemical polarization and improved rate capability. As demonstrated in carbonate electrolyte, the SeSPAN composite achieves a significantly

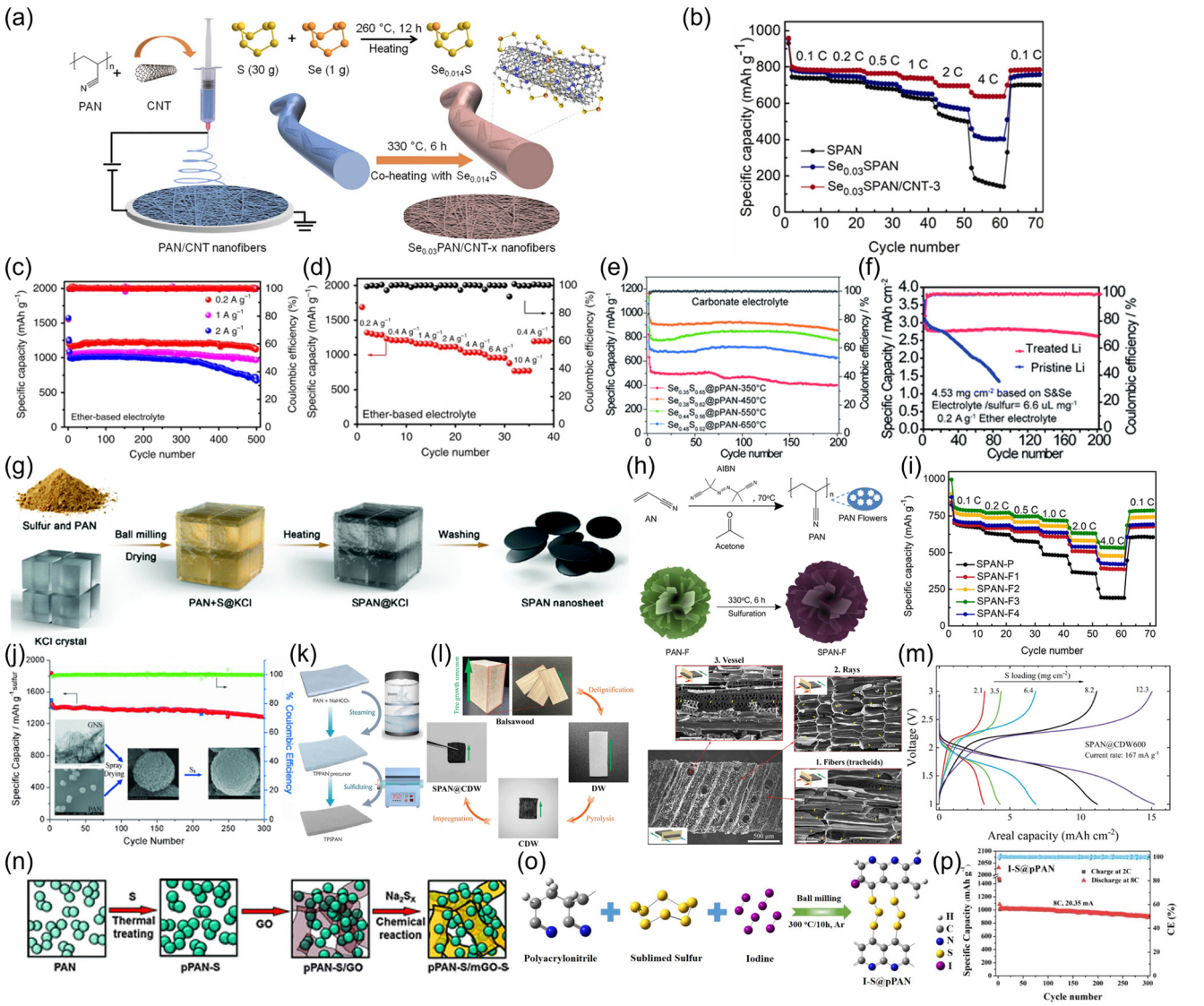

Fig. 7 Selenium doping and structural innovations in SPAN cathodes for high-performance Li–S batteries. (a and b) Se-doped fibrous SPAN/CNT composites improve Li^+ diffusion, enabling fast kinetics and stable cycling. Reproduced with permission from ref. 72. Copyright 2022, Elsevier. (c and d) Optimized Se content in the $Se_{0.06}$SPAN cathode enhances rate capability and long-term stability in ether-based electrolytes. Reproduced with permission from ref. 73. Copyright 2019, Springer Nature. (e and f) Se_xS_{1-x}@pPAN composites under optimized calcination deliver high capacity and areal performance under lean electrolyte and high-loading conditions. Reproduced with permission from ref. 74. Copyright 2020, Royal Society of Chemistry. (g) 2D SPAN nanosheets exhibit improved ion/electron transport and cycle life. Reproduced with permission from ref. 75. Copyright 2021, Royal Society of Chemistry. (h and i) 3D flower-like SPAN-F boosts sulfur content, rate performance, and structural adaptability. Reproduced with permission from ref. 76. Copyright 2023, American Chemical Society. (j) Hierarchical SPAN@GNS composites ensure high-rate operation and cycling retention. Reproduced with permission from ref. 77. Copyright 2014, Wiley-VCH. (k) Porous TPSPAN cathodes offer excellent shuttle suppression and long-cycle stability. Reproduced with permission from ref. 78. Copyright 2021, Elsevier. (l and m) Biobased SPAN@CDW achieves ultrahigh sulfur loading and areal capacities. Reproduced with permission from ref. 79. Copyright 2023, American Chemical Society. (n) Dual-mode pPAN-S/mGO-S structure integrates benefits of both sulfur hosts, improving capacity and CE. Reproduced with permission from ref. 80. Copyright 2012, Royal Society of Chemistry. (o and p) Iodine-doped I-S@pPAN enhances CEI formation, rate capability, and cycle life. Reproduced with permission from ref. 81. Copyright 2021, Elsevier.

© 2025 The Author(s). Published by the Royal Society of Chemistry

Open Access Article. Published on 15 July 2025. Downloaded on 6/21/2026 12:44:31 AM. This article is licensed under a Creative Commons Attribution 3.0 Unported Licence.

higher specific capacity (838 mA h g^{-1}) and longer cycle life than undoped SPAN, reflecting the beneficial impacts of Se doping on material structure and electrochemical stability.[71] Selenium-doped SPAN fiberous composites ($Se_{0.03}$SPAN/CNT; Fig. 7a) effectively enhanced lithium-ion diffusion and redox kinetics, delivering outstanding rate capability (638 mA h g^{-1} at 4C; Fig. 7b) and excellent cycle stability (capacity retention rate of 95.6% after 200 cycles at 0.2C).[72]

Further optimization of selenium content in SeSPAN cathodes has shown distinct benefits in both carbonate- and ether-based electrolytes. The introduction of a small catalytic amount of selenium ($Se_{0.06}$SPAN, ~50 wt% Se_xS) significantly accelerates reaction kinetics and effectively suppresses polysulfide dissolution, achieving outstanding performance particularly in ether-based electrolytes.[73] Fig. 7c and d display the $Se_{0.06}$SPAN composite delivers a remarkable reversible capacity of 1680 mA h g^{-1} at 0.2 A g^{-1}, maintaining 900 mA h g^{-1} even at high rates (10 A g^{-1}), highlighting the excellent rate capability.[73] Its long-term cycling stability with minimal capacity decay (0.029% per cycle over 800 cycles) further highlights selenium's effectiveness in facilitating rapid and complete conversion of polysulfide intermediates into insoluble Li_2S, a critical mechanism for enhancing electrolyte compatibility and battery longevity.[73]

Exploring the impact of calcination temperature on Se_xS_{1-x}@pPAN composites reveals a complex interplay between active material content, morphology, electrochemical polarization, and ion/electron transport capabilities.[74] Optimal calcination conditions (450 °C) produce the $Se_{0.38}S_{0.62}$@pPAN composite, demonstrating the best overall electrochemical performance, as shown in Fig. 7e.[74] This composite balances a moderate active material content with superior morphology, achieving lower polarization (0.42 V overpotential) and higher lithium-ion diffusion rates, essential for enhanced battery performance. It exhibits robust cycling stability in both carbonate and ether electrolytes, delivering capacities of 1163.5 mA h g^{-1} initially and maintaining 857.4 mA h g^{-1} after 200 cycles in carbonate electrolyte. Even under stringent conditions (high sulfur loading of 4.53 mg cm^{-2} and lean electrolyte conditions), the composite achieves an admirable areal capacity of 2.62 mA h cm^{-2} (Fig. 7f), reflecting its potential for practical Li–S battery applications.[74]

Overall, selenium doping in SPAN-based cathodes consistently demonstrates significant improvements in sulfur utilization, cycling stability, and rate performance across various electrolytes and operational conditions. This strategy not only resolves fundamental limitations associated with polysulfide dissolution but also enhances electronic conductivity and reaction kinetics. Other approaches, such as transition metal coordination (*e.g.*, $CoSe_2$, Co–N_4S, and FeCo) to introduce catalytic activity and conductive pathways, have also shown promise.[82–84] However, given the wide variety of transition metals and coordination environments reported, a dedicated review is needed to systematically clarify their mechanisms and classifications.

4.5 Architecturally tailored SPAN composites with special morphologies

Architecturally engineered and morphologically innovative SPAN composites have been shown to significantly enhance electrochemical performance by improving sulfur utilization, rate capability, and cycling stability through optimized electron/ion transport and active material accessibility. This subsection focuses on representative structural design strategies that have demonstrated consistent performance benefits, such as 2D/3D architectures, hierarchical porosity, and templated morphologies. Two-dimensional SPAN nanosheets prepared by inorganic salt templating (Fig. 7g) provide a large electrode–electrolyte contact area and shorter transport paths for electrons and ions.[75] Compared to conventional SPAN nanoparticles, nanosheets exhibit higher discharge capacities and superior rate performance. Specifically, SPAN nanosheets demonstrate capacities of 484 mA h g^{-1} after 300 cycles at 0.2 A g^{-1} (76.8% retention) and 408 mA h g^{-1} after 100 cycles at 2 A g^{-1} (95% retention). Electrochemical impedance spectroscopy (EIS) and diffusion coefficient analysis confirm enhanced charge transfer and lithium-ion diffusion kinetics.[75] Additionally, nanosheets maintain excellent performance under lean electrolyte conditions and in practical pouch cells, indicating suitability for real-world applications. A novel three-dimensional flower-shaped SPAN (SPAN-F) composite was developed to address SPAN's low sulfur content and sluggish kinetics (Fig. 7h).[76] This structure significantly improves sulfur content and electrochemical properties. The optimized SPAN-F3 cathode achieves an exceptional capacity of 789 mA h g^{-1} at 0.2C, remarkable rate performance (571 mA h g^{-1} at 4C; Fig. 7i), and outstanding cycling stability (673 mA h g^{-1} after 500 cycles at 1C).[76] The unique 3D flower-like structure effectively facilitates lithium-ion transport, adapts to volume changes, and minimizes polarization, enhancing the electrode's overall electrochemical stability and capacity retention, even under high mass loading (8.6 mg cm^{-2}) and lean electrolyte conditions.[76] In another approach to improve sulfur loading and capacity, a cross-linked PAN (CPAN) precursor with a porous structure and high surface area was synthesized *via* an intermolecular cross-linking strategy.[85] This design enables the S@pPAN composite to reach a sulfur content of 53.36 wt% and deliver a high reversible capacity of 829 mA h g^{-1} with 92.9% sulfur utilization, offering a promising route toward high-energy-density Li–S batteries.[85]

Hierarchically structured SPAN@GNS composites synthesized *via* spray drying significantly enhance the electrochemical performance by assembling PAN nanoparticles uniformly within a conductive GNS network.[77] This composite structure maintains excellent rate capability, delivering approximately 700 mA h g^{-1} (sulfur basis) even at a high discharge rate of 10C. It also achieves outstanding cycling stability with 88.8% capacity retention over 300 cycles at 0.2C (Fig. 7j).[77] The spherical and hierarchical structure of SPAN@GNS composites ensures improved electronic

Open Access Article. Published on 15 July 2025. Downloaded on 6/21/2026 12:44:31 AM. This article is licensed under a Creative Commons Attribution 3.0 Unported Licence.

conductivity, structural integrity, and interfacial stability, providing a scalable strategy for practical applications.[77,86–88] Three-dimensional porous SPAN (TPSPAN), fabricated *via* a steaming process using sodium bicarbonate as a space-holder (Fig. 7k), offers enhanced electrochemical characteristics through its interconnected porous network.[78] This porous structure significantly mitigates polysulfide shuttle effects, improves electrode wettability, and accelerates ionic transport. TPSPAN cathodes deliver outstanding performance, achieving capacities of 1304 mA h g^{-1} at 0.1 A g^{-1}, maintaining excellent rate capability (986 mA h g^{-1} at 2.0 A g^{-1}), and exhibiting remarkable cycling stability (94.6% retention after 1000 cycles at 2.0 A g^{-1}), thus demonstrating a scalable strategy for advanced cathode material development.[78] The freestanding SPAN-impregnated carbonized delignified wood (SPAN@CDW) electrode demonstrates exceptional high-areal capacity performance due to its biobased 3D porous architecture (Fig. 7l).[79] The interconnected porous structure significantly enhances electron/ion transport, enabling high sulfur loadings up to 35 mg cm^{-2} and achieving remarkable capacities exceeding 1000 mA h g^{-1} at 1C.[79] The SPAN@CDW electrode maintains 85% capacity retention (1344 mA h g^{-1}) after 500 cycles, highlighting excellent long-term stability. Moreover, at high sulfur loadings (12.3 mg cm^{-2}), it attains an impressive areal capacity of 15.13 mA h cm^{-2} (Fig. 7m), positioning CDW-based electrodes as sustainable, high-performance cathodes for practical Li–S battery applications.[79]

A dual-mode sulfur-based cathode (pPAN-S/mGO-S) integrates sulfur within both pyrolyzed polyacrylonitrile (pPAN) nanoparticles and mildly reduced graphene oxide (mGO) nanosheets, exhibited in Fig. 7n, significantly improving sulfur content, utilization, and cycling stability.[80] This structure achieves an initial reversible capacity of 1400 mA h g^{-1} (sulfur basis) with stable cycling around 650 mA h g^{-1} (composite) and enhanced coulombic efficiency above 98%. The dual-mode approach effectively combines advantages of pPAN-S and mGO-S, enhancing electrochemical performance and providing a promising pathway for future Li–S battery designs.[80] Another unique iodine-doped sulfurized polyacrylonitrile (I-S@pPAN; Fig. 7o) structure was developed through a simple co-heating approach, significantly enhancing electrochemical performance in carbonate-based electrolytes.[81] Iodine doping markedly improves electron and lithium-ion conductivity, accelerating reaction kinetics and forming a robust cathode electrolyte interface (CEI) layer rich in LiF and LiI.[81] The I-S@pPAN cathode delivers a high reversible capacity of 1267 mA h g^{-1} at 2C, maintaining 85% retention after 1000 cycles. Even at extreme rates (8C), it exhibits capacities of 1085 and 792 mA h g^{-1} after 300 cycles (Fig. 7p), demonstrating outstanding rate capability and cycling performance.[81] Finally, introducing nanostructured magnesium nickel oxide ($Mg_{0.6}Ni_{0.4}O$) into SPAN composites significantly improves sulfur utilization, morphology stability, and electrochemical kinetics.[89] This additive, synthesized *via* self-propagating high-temperature synthesis (SHS), reduces polarization and enhances conductivity, resulting in high initial reversible capacities (1223 mA h g^{-1}), excellent cycling stability (100% retention over 100 cycles), and significantly improved rate capability.[89] Thus, $Mg_{0.6}Ni_{0.4}O$ emerges as a promising additive to enhance SPAN cathodes for practical high-energy Li–S battery applications.[89]

These innovative structural strategies provide robust solutions to address intrinsic limitations in SPAN cathodes, advancing their practical viability in high-performance Li–S batteries. To provide a consolidated overview, Table 1 summarizes recent SPAN-based cathode systems discussed in this review, including their specific capacities, cycling performance, rate capabilities, electrolyte systems, S : PAN precursor ratios, synthesis temperatures, sulfur contents, and electrolyte-to-sulfur (E/S) ratios.

5. Electrolytes and binders for SPAN cathodes

Electrolytes and binders also play critical roles in enhancing the electrochemical performance, cycling stability, and safety of SPAN cathodes. In particular, the development of non-flammable electrolytes is increasingly recognized as a crucial direction for improving battery safety,[90] especially for practical applications beyond laboratory settings. In parallel, various strategies involving electrolyte optimization and novel binder systems have been developed to address intrinsic challenges, such as polysulfide dissolution, electrolyte compatibility, and structural integrity during cycling.

A multi-system adaptable gel polymer electrolyte (PFGPE), synthesized *via in situ* polymerization of pentaerythritol tetraacrylate (PETEA) and hexafluorobutyl acrylate (HFBA), significantly improves interfacial stability and polysulfide suppression in both ether- and carbonate-based Li-SPAN batteries (Fig. 8a).[91] The PFGPE forms robust CEI and solid electrolyte interphase (SEI) layers, facilitating rapid Li^+ transport and stable cycling.[91] Ether-based SPAN/PFGPE cells exhibit exceptional long-term stability, maintaining a capacity of 725.1 mA h g^{-1} after 600 cycles at 0.2C (Fig. 8b).[91] Similarly, in ester-based systems, PFGPE ensures a remarkable capacity retention of 1324.24 mA h g^{-1} after 200 cycles at 0.1C (Fig. 8c), significantly outperforming conventional liquid electrolytes.[91] Additionally, the electrolyte demonstrates high ionic conductivity (1.61 mS cm^{-1}) and extended Li||Li symmetric cell lifetimes, indicating its broad applicability and effectiveness.[91]

The role of carbonate electrolyte viscosity was systematically investigated in a previous report, revealing a clear correlation between lower viscosity and enhanced electrochemical performance.[26] Using linear symmetric carbonates such as dimethyl carbonate (DMC), diethyl carbonate (DEC), dipropyl carbonate (DPC), and ethylene glycol bis(methyl carbonate) (EGBMC), it was found that lower viscosity electrolytes, compared in Fig. 8d, particularly DMC-based formulations, achieved superior

© 2025 The Author(s). Published by the Royal Society of Chemistry

Open Access Article. Published on 15 July 2025. Downloaded on 6/21/2026 12:44:31 AM.
This article is licensed under a Creative Commons Attribution 3.0 Unported Licence.

Table 1 Summary of recent studies on SPAN cathodes for lithium–sulfur batteries, highlighting specific capacity, cycling performance, capacity retention, rate capability, areal sulfur loading, electrolyte systems, and S : PAN ratios

Capacity (mA h g^{-1})	Cycle number	Capacity retention (%)	Highest C-rate/capacity (mA h g^{-1})	Areal density (mg cm^{-2})	Electrolyte	S : PAN ratio	Syn. temp. (°C)	S cont. (%)	E/S ratio (μL mg^{-1})	Ref.
2207	100	98.4 (200 mA g^{-1})	—	2.5	1 M $LiPF_6$ in EC : DEC : DMC = 1 : 1 : 1 (v : v : v)	3 : 1	350	37.64	—	28
1530	100	98.5 (0.5C)	3C/1000	3	1 M $LiPF_6$ in EC/DEC = 1 : 1 (v : v) with 5 wt% FEC	—	350	45	—	29
1843	1000	—	1.6C/1000	0.85	1 M $LiPF_6$ in EC/DEC = 1 : 1 (v : v)	4 : 1	450	—	—	30
~800	2000	96.8 (0.5 A g^{-1})	5 A g^{-1}/444	1.5	1 M $LiPF_6$ in EC/DEC = 1 : 1 (v : v)	—	330	—	—	31
~12 mA h cm^{-3}	100	~70	1 mA cm^{-2}/12 mA h cm^{-3}	10.1	1.8 M LiFSI in DME/TTE = 1.2 : 4 (v : v)	3 : 1	450	40.99	2.2	32
1801	250	~82.3 (0.1C)	2C/353	0.86	1 M $LiPF_6$ in EC/DEC = 1 : 1 (v : v)	4 : 1	350	48	—	34
984	50	98.1	—	—	1 M $LiPF_6$ in EC/DMC/EMC = 1 : 1 : 1 (v : v : v)	—	350	42	—	35
~1700	50	—	10C/800 mA h	—	1 M $LiPF_6$ in EC/DEC = 1 : 1 (v : v) 1 M LiTFSI in DOL/DME = 1 : 1 (v : v)	4 : 1	350	44.7	—	39
~1000	200	84.4 (160 mA g^{-1})	4C/370	1	1 M $LiPF_6$ in EC/PC/DEC = 4 : 1 : 5 (v : v : v)	6 : 1	300	52	—	46
~900	100	—	—	—	1, 3, 5 M LiTFSI in DOL/DME = 1 : 1 (v : v) 1, 3, 5 M LiTFSI in DOL/TEGDME = 1 : 1 (v : v)	4 : 6	350	56	—	47
870.7	50	~75.6 (0.2 mA)	0.5/500	—	1 M $LiPF_6$ in EC/DEC = 1 : 1 (v : v)	—	300	46.85	—	48
1416	200	~72.4	1C/933	2.5	1 M $LiPF_6$ in EC/DMC = 1 : 1 (v : v)	0.2 : 4	450	—	—	49
907.4	200	92.4 (0.2C)	4C/207.2	—	1 M $LiPF_6$ in EC/DMC = 1 : 1 (v : v)	7 : 1	330	—	—	50
706.8	100	~96.47 (0.5C)	7C/386.7	4	1 M $LiPF_6$ in EC/DMC = 1 : 1 (v : v)	10 : 1	300	35.1	—	51
~820	50	85 (0.1C)	4C/260	—	1 M $LiPF_6$ in EC/DMC = 1 : 1 (v : v)	7 : 1	300	—	—	52
1850	100	80 (0.1C)	6C/800	—	1 M $LiPF_6$ in EC/DMC = 1 : 1 (v : v)	—	300	47	—	54
1827	200	80 (0.1C)	2C/828	6–8	1 M $LiPF_6$ in EC/DMC/DC = 1 : 1 : 1 (v : v : v)	4 : 1	320	44	—	55
1652	100	72.2 (0.1C)	1C/946	2.05	0.7 M LiTFSI in DME/DOL = 1 : 1 (v : v) with 0.05 M $LiNO_3$	4 : 1	155	55.4	—	57
1178.9	800	~91.8 (0.5C)	5C/494.8	15.2	0.7 M LiTFSI in DME/DOL = 1 : 1 (v : v) with 1 wt% $LiNO_3$	4 : 1	155	40.2	18	58
~2750	300	80 (0.25C)	1C/600	10	1 M $LiPF_6$ in EMC/FEC = 3 : 1 (v : v) 1 M LiDFOB in EMC/FEC = 3 : 1 (v : v)	4 : 1	450	46.5	12	59
2172	500	90 (0.5C)	5C/1130	0.6	1 M $LiPF_6$ in EC/DEC/FEC = 4.5 : 4.5 : 1 (v : v : v)	3 : 1	350	33.6	—	60
1782.4	300	70 (0.1C)	1C/499	2.2	1 M LiTFSI in DME/DOL = 1 : 1 (v : v) with 1 wt% $LiNO_3$	3 : 1	390	41.19	—	61
1814	150	~49.8 (0.1C)	4C/300	6.37	1 M $LiPF_6$ in EC/DEC = 1 : 1 (v : v)	—	350	37.78	—	62
1692	100	~67.6 (0.2C)	2C/794	—	1 M $LiPF_6$ in EC/PC/DEC = 4 : 1 : 5 (v : v : v)	—	300	48	—	63
1672	1200	~48 (2C)	8C/380	—	3 M LiTFSI in FEC/DOL = 1 : 1 (v : v)	—	550	46	—	64
1416	200	96.8 (0.2C)	2C/1159	—	1 M $LiPF_6$ in EC/DEC = 1 : 1 (v : v)	6 : 1	330	53	40	65
1332	500	~96.17 (1 A g^{-1})	5 A g^{-1}/141.7	1–1.2	1 M LiTFSI in DOL/DME = 1 : 1 (v : v) 1 M $LiPF_6$ in EC/DEC = 1 : 1 (v : v)	6 : 1	600	45	—	66
1799	100	~69 (0.2C)	5C/223	2.4	1 M $LiPF_6$ in EC/DEC/DMC = 1 : 1 : 1 (v : v : v)	10 : 1	400	43.2	25	67
967	500	~64.4 (0.2C)	2C/303	1	1 M $LiPF_6$ in EC/DEC = 1 : 1 (v : v) with 10% FEC	5 : 1	350	33.2	15	68
1301	400	99.05 (0.1C)	2C/660	0.86–1.2	1 M $LiPF_6$ in EC/DEC = 1 : 1 (v : v)	4 : 1	350	58	—	69
1814	200	~70.56 (400 mA g^{-1})	1.6 A g^{-1}/810	—	1 M LiTFSI in DME/DOL = 1 : 1 (v : v) with 0.2 M $LiNO_3$	—	500	46.64	—	70
1044	250	80 (0.1 A g^{-1})	2 A g^{-1}/600	1	1 M $LiPF_6$ in EC/DEC = 1 : 1 (v : v)	3 : 1	300	60	—	71
952	200	95.6 (0.2C)	4C/638	1–1.4	1 M $LiPF_6$ in EC/DMC = 1 : 1 (v : v) with 10% FEC	6 : 1	330	51.73	40	72
1680	500	91.6 (0.2 A g^{-1})	6.5C/900	1–3	1 M LiTFSI in DME/DOL = 1 : 1 (v : v) with 2 wt% $LiNO_3$	3 : 1	300	47.25	—	73
1112.2	200	~72.47 (0.4 A g^{-1})	3 A g^{-1}/764.8	2	1 M $LiPF_6$ in EC/DEC = 1 : 1 (v : v) 1 M LiTFSI in DME/DOL = 1 : 1 (v : v) with 2 wt% $LiNO_3$	3 : 1	450	54.79	—	74

© 2025 The Author(s). Published by the Royal Society of Chemistry

Open Access Article. Published on 15 July 2025. Downloaded on 6/21/2026 12:44:31 AM.
This article is licensed under a Creative Commons Attribution 3.0 Unported Licence.

Table 1 *(continued)*

Capacity ($mA\ h\ g^{-1}$)	Cycle number	Capacity retention (%)	Highest C-rate/capacity ($mA\ h\ g^{-1}$)	Areal density ($mg\ cm^{-2}$)	Electrolyte	S:PAN ratio	Syn. temp. (°C)	S cont. (%)	E/S ratio ($\mu L\ mg^{-1}$)	Ref.
~670	100	95 (0.2 $A\ g^{-1}$)	5 $A\ g^{-1}$/484	1.8	1 M $LiPF_6$ in EC/DEC = 1 : 1 (v : v)	4 : 1	350	46	10	75
961	200	98.5 (0.2C)	2C/688	2.4–2.6	1 M $LiPF_6$ in EC/DEC = 1 : 1 (v : v) with 15% FEC	7 : 1	330	52.8	20	76
1840	300	88.8 (0.2C)	10C/700	2	1 M $LiPF_6$ in EC/DEC = 1 : 1 (v : v)	7 : 1	300	47	—	77
1304	1000	94.6 (2 $A\ g^{-1}$)	2 $A\ g^{-1}$/986	—	1 M $LiPF_6$ in EC/DEC = 1 : 1 (v : v)	3 : 1	350	—	—	78
~2250	500	~85 (167 $A\ g^{-1}$)	1C/1200	2.1	1 M LiTFSI in EC/DME/DOL = 2 : 1 : 1 (v : v : v)	3 : 1	600	34.8	25	79
~1100	50	~59 (0.1C)	—	—	1 M LiTFSI in DME/DOL = 1 : 1 (v : v)	—	300	65.1	—	80
1591	1000	85 (2C)	8C/533	2.3	1 M $LiPF_6$ in EC/DMC = 3 : 7 (v : v) with 5% FEC	3.4 : 1	300	48.5	49	81
1856	1500	81.5 (1C)	10C/350	1	1 M $LiPF_6$ in EC/DEC/DMC = 1 : 1 : 1 (v : v : v)	10 : 1	400	—	—	83
1038	200	91 (0.2C)	0.2C/744	1	1 M $LiPF_6$ in EC/DMC = 1 : 1 (v : v)	8 : 1	300	53.63	—	85
1545	100	79.2 (0.1C)	1C/450	4	1 M $LiPF_6$ in EC/DEC/DMC = 1 : 1 : 1 (v : v : v)	4 : 1	350	38.5	—	89
~2150	1000	78.1 (1C)	4C/~900	1	1 M LiBOB/TPE + FEC = 7 : 3 (v : v)	8 : 1	300	44.5	—	90
1237.5	600	58.5 (0.2C)	1C/444.75	0.63	PFGPE	4 : 1	450	—	—	91
~1850	40	92.4	—	17.5	1 M $LiPF_6$ in FEC/DMC = 1 : 1 (v : v)	8 : 1	300	44.5	—	92
—	100	—	8C/~700	0.6	3 M LiTFSI in FEC/DMC = 2 : 1 (v : v)	—	—	41.4	—	93
1169.9	100	74 (500 $mA\ g^{-1}$)	—	1.5	1 M $LiPF_6$ in EC/DEC/DMC = 1 : 1 : 1 (v : v : v)	—	280–300	50	—	99

capacities.[26] Specifically, SPAN cells employing 3 M LiTFSI in fluorinated ethylene carbonate (FEC)/DMC (2 : 1) achieved high reversible capacities of 990 mA h g^{-1} after 600 cycles at 0.5C.[26] The optimal combination of DMC and cyclic carbonates (FEC, ethylene carbonate (EC)) significantly enhances cell performance and longevity, highlighting the importance of electrolyte composition in improving SPAN-based battery performance.[26]

Temperature-dependent performance studies further emphasized electrolyte viscosity effects, investigating four carbonate-based electrolytes containing FEC or EC with varying salt concentrations.[93] These studies demonstrated reversible cycling behavior between −20 °C and 38 °C, with rapid and irreversible capacity fading above 38 °C.[93] Low-temperature performance was limited by increased electrolyte viscosity, yet cells fully recovered upon returning to room temperature. FEC-based electrolytes particularly exhibited superior low-temperature stability compared to EC-based counterparts, highlighting the necessity of balancing viscosity and electrolyte composition for optimal thermal performance.[93]

Beyond conventional carbonate and ether solvents, a recent study introduced a non-flammable acetonitrile (AN)-based electrolyte stabilized with FEC, enabling long-term cycling of SPAN cathodes in both Li||SPAN and graphite||SPAN cells.[94] The FEC additive was found to inhibit C–S bond cleavage and suppress the formation of elemental sulfur, thus preserving the SPAN structure and forming a stable cathode electrolyte interphase. This system achieved 900 cycles in Li||SPAN and 1500 cycles with 91% capacity retention in graphite||SPAN full cells, marking a significant advance toward safer, practical SPAN-based batteries.[94]

In addition to electrolyte advancements, novel binder systems significantly influence electrode performance by enhancing structural integrity and ionic transport. A crosslinked binder combining guar gum (GG) and poly(acrylic acid) (PAA) was developed to fabricate high-loading S@pPAN cathodes with superior mechanical stability and electrochemical performance (Fig. 8e).[92] Utilizing industrial rolling for electrode compaction, a remarkable sulfur loading of 6.23 mg cm^{-2} was achieved, delivering a stable areal capacity of 6 mA h cm^{-2} after 120 cycles.[92] Although electrode compaction significantly improved electronic and ionic transport, excessive compaction (>10 MPa) hindered electrolyte penetration, reducing capacity due to poor electrode wetting.[92] Detailed analysis indicated battery failure was mainly due to lithium anode degradation rather than cathode structural issues, highlighting the importance of comprehensive battery optimization, including electrolyte–anode interface management.[92]

As a result, these studies highlight the critical roles of optimized electrolyte formulations and innovative binder designs in enhancing SPAN cathode performance. Such strategies effectively address electrolyte compatibility, polysulfide suppression, and structural integrity.

© 2025 The Author(s). Published by the Royal Society of Chemistry

Open Access Article. Published on 15 July 2025. Downloaded on 6/21/2026 12:44:31 AM.
This article is licensed under a Creative Commons Attribution 3.0 Unported Licence.

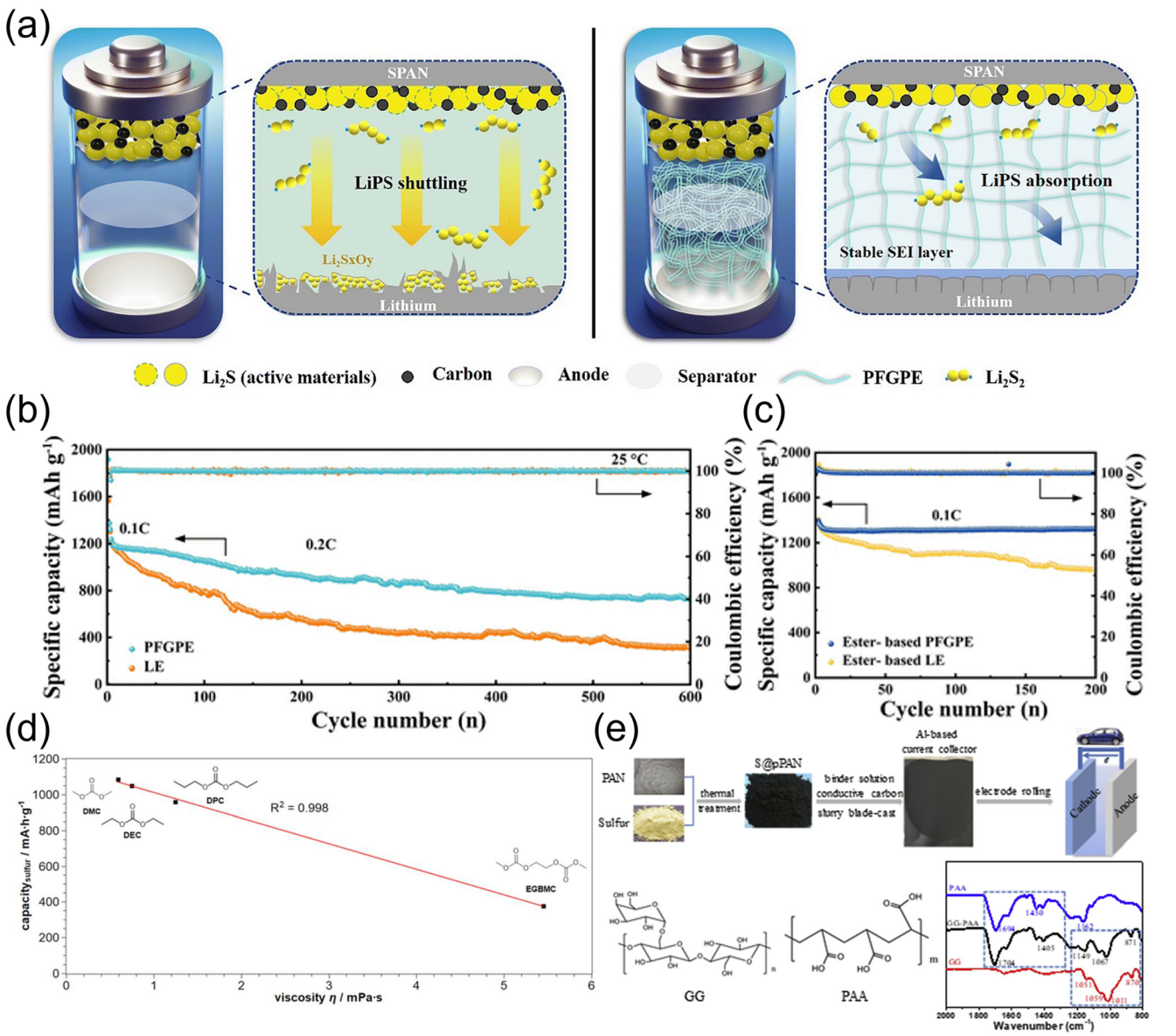

Fig. 8 Electrolyte and binder optimization for enhanced SPAN cathode performance. (a–c) Multi-system adaptable gel polymer electrolyte (PFGPE), synthesized *via in situ* polymerization of PETEA and HFBA, effectively stabilizes the cathode–electrolyte interface in both ether- and carbonate-based electrolytes, achieving superior cycling stability and ionic conductivity. Reproduced with permission from ref. 91. Copyright 2024, Royal Society of Chemistry. (d) Influence of carbonate electrolyte viscosity on SPAN cathode performance highlights superior electrochemical stability and capacity retention with lower-viscosity DMC-based electrolytes. Reproduced with permission from ref. 26. Copyright 2018, IOP Publishing. (e) Crosslinked guar gum/poly(acrylic acid) binder facilitates high sulfur loading and structural integrity, enhancing areal capacity and cycling performance through optimized electrode compaction conditions. Reproduced with permission from ref. 92. Copyright 2020, Elsevier.

6. Li-SPAN pouch cells and practical implementation

Although SPAN cathodes are primarily investigated in coin-type cells, several recent studies have demonstrated their viability in pouch cell formats. A flexible pouch cell using hollow tubular SPAN fiber electrodes (H-SPAN) achieved a stable capacity of 1100 mA h g^{-1} over 50 cycles with excellent mechanical integrity under repeated bending, demonstrating strong potential for wearable electronics.[95] Nanosheet-structured SPAN enabled compact pouch cells with reversible capacity of 362.8 mA h g^{-1} and nearly 100% capacity retention over 100 cycles at 0.2 A g^{-1}, thanks to enhanced redox kinetics and ion/electron transport.[96] In another study, combining sulfurized carbonized PAN with a PAA binder and FEC additive led to pouch cells with 97.5% capacity retention after 100 cycles at 0.5 C and 3.0 mg cm^{-2} sulfur loading, with successful scale-up to 260 mA h.[97] Further performance improvements were achieved using a CoS_2-anchored SPAN-CNT film, enabling 1322 mA h g^{-1} in a flexible pouch configuration with high sulfur loading (5.9 mg cm^{-2}) and areal capacity of 8.1 mA h cm^{-2}.[98] Notably, a lithium-free full-

Open Access Article. Published on 15 July 2025. Downloaded on 6/21/2026 12:44:31 AM. This article is licensed under a Creative Commons Attribution 3.0 Unported Licence.

cell design using pre-lithiated SPAN cathodes and Si/C anodes *via* a nitrogen evolution reaction yielded 513.2 Wh kg^{-1} at 4.2 mg cm^{-2} sulfur loading, offering a promising high-energy-density alternative to conventional Li–S systems.[99] These advancements confirm the practical potential of SPAN-based cathodes and suggest viable routes toward scalable, safe, and high-energy Li–S pouch cells.

7. Considerations and future directions

The development of SPAN-based cathodes has shown remarkable progress, yet several critical considerations must be addressed to further advance practical applications. Key aspects include enhancing sulfur content, optimizing electrode structures, and advancing compatible electrolyte systems. Future research should prioritize strategies that simultaneously achieve high sulfur loading and stable cycling performance under realistic battery conditions, including lean electrolyte and high areal loading.

A promising area involves molecular-level doping and heteroatom incorporation to enhance intrinsic conductivity and reaction kinetics. Exploration of synergistic doping, such as dual-element strategies (*e.g.*, selenium–iodine or selenium–nitrogen), could potentially overcome current limitations in conductivity and polysulfide management. Advanced computational techniques, including machine learning and high-throughput DFT screening, could rapidly identify optimal doping configurations and compositions. Additionally, innovative electrolyte engineering remains crucial, particularly in developing electrolytes tailored explicitly for SPAN systems. Future work should explore novel solvents and electrolyte additives that stabilize electrode–electrolyte interfaces, minimize polysulfide dissolution, and improve low-temperature performance. Developing solid-state electrolytes compatible with SPAN cathodes could further enhance battery safety and performance stability.

Scale-up studies and pouch-cell demonstrations under commercially relevant conditions will be essential to translate laboratory advancements to practical energy storage solutions. Integration of sustainable and cost-effective materials, such as biomass-derived carbon supports or recyclable electrolytes, could enhance environmental friendliness and economic viability. Addressing these critical areas will undoubtedly expand SPAN cathode viability in next-generation Li–S batteries, meeting diverse energy storage demands.

8. Conclusions

Significant advancements in SPAN-based cathode materials have been achieved through comprehensive structural characterization, innovative composite designs, and strategic doping. The unique molecular structure of SPAN, characterized by covalently bonded sulfur to polyacrylonitrile-derived carbon backbones enriched with conjugated bonds, underpins its robust solid-phase lithium storage mechanism. This structure effectively mitigates polysulfide dissolution and enhances cycling stability compared to traditional sulfur cathodes.

Carbon-based composites, including engineered porous structures, graphene integration, and catalytic metal sulfides, have substantially improved electron and ion transport, active material utilization, and electrochemical stability. Selenium doping strategies and specialized morphological designs further address intrinsic conductivity limitations, significantly enhancing sulfur utilization and rate capabilities. Electrolyte and binder innovations have critically supported the performance of SPAN cathodes, emphasizing optimized electrolyte formulations, gel-polymer electrolytes, and advanced binders for enhanced mechanical stability and ionic transport. However, future developments must address remaining challenges, including achieving higher sulfur loadings, electrolyte compatibility improvements, and practical scalability.

Continued exploration into doping strategies, electrolyte systems, and sustainable materials will be key to realizing full potential of SPAN cathodes. Such focused research will position SPAN-based lithium–sulfur batteries as competitive candidates for diverse and demanding energy storage applications, marking a significant advancement in battery technology.

Data availability

All data supporting the findings of this review are cited from published sources and reproduced with permission where applicable. No new data were generated in this study.

Conflicts of interest

There are no conflicts to declare.

Acknowledgements

This research was funded by the National Science and Technology Council (NSTC) of Taiwan (113-2628-E-A49-011) and by the Ministry of Education (MOE) of Taiwan under the Yushan Young Fellow Program and Higher Education SPROUT Project of National Yang Ming Chiao Tung University.

References

1 A. Manthiram, Y. Fu and Y.-S. Su, *Acc. Chem. Res.*, 2013, **46**, 1125–1134.
2 P. G. Bruce, S. A. Freunberger, L. J. Hardwick and J.-M. Tarascon, *Nat. Mater.*, 2012, **11**, 19–29.
3 L. Zhou, D. L. Danilov, R. Eichel and P. H. L. Notten, *Adv. Energy Mater.*, 2021, **11**, 2001304.
4 K. Chiu, A. L. Bhat, C. Yang, S. Chung, N. Tumilty and Y. Su, *Small*, 2024, 2405365.
5 Y.-S. Su, Y. Fu, T. Cochell and A. Manthiram, *Nat. Commun.*, 2013, **4**, 2985.
6 Y. Su, Y. Fu, B. Guo, S. Dai and A. Manthiram, *Chem. – Eur. J.*, 2013, **19**, 8621–8626.

© 2025 The Author(s). Published by the Royal Society of Chemistry

Open Access Article. Published on 15 July 2025. Downloaded on 6/21/2026 12:44:31 AM. This article is licensed under a Creative Commons Attribution 3.0 Unported Licence.

7 M. J. Lacey, A. Yalamanchili, J. Maibach, C. Tengstedt, K. Edström and D. Brandell, *RSC Adv.*, 2016, **6**, 3632–3641.
8 P. Yu, S. Sun, C. Sun, C. Zeng, Z. Hua, N. Ahmad, R. Shao and W. Yang, *Adv. Funct. Mater.*, 2024, **34**, 2306939.
9 M. Yu, Z. Wang, Y. Wang, Y. Dong and J. Qiu, *Adv. Energy Mater.*, 2017, **7**, 1700018.
10 T. A. N. Bui and Y.-S. Su, *J. Power Sources*, 2025, **627**, 235828.
11 Y.-S. Su and A. Manthiram, *Chem. Commun.*, 2012, **48**, 8817.
12 Y.-S. Su and A. Manthiram, *Nat. Commun.*, 2012, **3**, 1166.
13 P. Wang, X. Dai, P. Xu, S. Hu, X. Xiong, K. Zou, S. Guo, J. Sun, C. Zhang, Y. Liu, T. Zhou and Y. Chen, *eScience*, 2023, **3**, 100088.
14 Y. Du, Y. Liu, F. Cao and H. Ye, *Energy Mater.*, 2024, **4**, 400014.
15 A. L. Phan, P. M. L. Le and C. Wang, *Joule*, 2024, **8**, 1601–1618.
16 X. Zhao, C. Wang, Z. Li, X. Hu, A. Abdul Razzaq and Z. Deng, *J. Mater. Chem. A*, 2021, **9**, 19282–19297.
17 S. Zhang, *Energies*, 2014, **7**, 4588–4600.
18 X. Zhang, K. Chen, Z. Sun, G. Hu, R. Xiao, H.-M. Cheng and F. Li, *Energy Environ. Sci.*, 2020, **13**, 1076–1095.
19 Y. Hu, H. Cheng, H. Chen, S. Dai, K. Song, X. Ma, M. Liu and H. Hu, *J. Mater. Chem. A*, 2022, **10**, 22896–22914.
20 X. Wu, Y. Zhao, H. Li, C. Zhou, X. Wang and L. Du, *Nanoscale*, 2024, **16**, 5060–5078.
21 J. Wang, J. Yang, C. Wan, K. Du, J. Xie and N. Xu, *Adv. Funct. Mater.*, 2003, **13**, 487–492.
22 J. Wang, J. Yang, J. Xie and N. Xu, *Adv. Mater.*, 2002, **14**, 963–965.
23 M. S. Ahmed, S. Lee, M. Agostini, M. Jeong, H. Jung, J. Ming, Y. Sun, J. Kim and J. Hwang, *Adv. Sci.*, 2021, **8**, 2101123.
24 R. Mukkabla and M. R. Buchmeiser, *J. Mater. Chem. A*, 2020, **8**, 5379–5394.
25 L. Zhang, W. Zhang, Z. Zhu, Q. Huang, X. Liu, M. Zhang, W.-B. Pei and J. Wu, *J. Solid State Chem.*, 2021, **301**, 122359.
26 S. Warneke, A. Hintennach and M. R. Buchmeiser, *J. Electrochem. Soc.*, 2018, **165**, A2093–A2095.
27 T. Yim, M.-S. Park, J.-S. Yu, K. J. Kim, K. Y. Im, J.-H. Kim, G. Jeong, Y. N. Jo, S.-G. Woo, K. S. Kang, I. Lee and Y.-J. Kim, *Electrochim. Acta*, 2013, **107**, 454–460.
28 Z.-Q. Jin, Y.-G. Liu, W.-K. Wang, A.-B. Wang, B.-W. Hu, M. Shen, T. Gao, P.-C. Zhao and Y.-S. Yang, *Energy Storage Mater.*, 2018, **14**, 272–278.
29 H. M. Kim, J.-Y. Hwang, D. Aurbach and Y.-K. Sun, *J. Phys. Chem. Lett.*, 2017, **8**, 5331–5337.
30 S. Wei, L. Ma, K. E. Hendrickson, Z. Tu and L. A. Archer, *J. Am. Chem. Soc.*, 2015, **137**, 12143–12152.
31 W. Wang, Z. Cao, G. A. Elia, Y. Wu, W. Wahyudi, E. Abou-Hamad, A.-H. Emwas, L. Cavallo, L.-J. Li and J. Ming, *ACS Energy Lett.*, 2018, **3**, 2899–2907.
32 Z. Jiang, H.-J. Guo, Z. Zeng, Z. Han, W. Hu, R. Wen and J. Xie, *ACS Nano*, 2020, **14**, 13784–13793.
33 H. Cheng, Q. Sun, L. Li, Y. Zou, Y. Wang, T. Cai, F. Zhao, G. Liu, Z. Ma, W. Wahyudi, Q. Li and J. Ming, *ACS Energy Lett.*, 2022, **7**, 490–513.
34 M. A. Weret, C.-F. Jeffrey Kuo, T. S. Zeleke, T. T. Beyene, M.-C. Tsai, C.-J. Huang, G. B. Berhe, W.-N. Su and B.-J. Hwang, *Energy Storage Mater.*, 2020, **26**, 483–493.
35 L. Wang, X. He, J. Li, J. Gao, J. Guo, C. Jiang and C. Wan, *J. Mater. Chem.*, 2012, **22**, 22077.
36 H. Li, W. Xue, W. Xu, L. Wang and T. Liu, *Compos. Commun.*, 2021, **24**, 100675.
37 K. Yu, G. Cai, M. Li, J. Wu, V. Gupta, D. J. Lee, J. Holoubek and Z. Chen, *ACS Appl. Mater. Interfaces*, 2023, **15**, 43724–43731.
38 J. Liu, H. Lu, X. Kong, Y. Guan, Q. Wang, B. Chong, J. Yang, Y. NuLi, H. Duan and J. Wang, *Adv. Mater.*, 2025, 2503534.
39 C.-J. Huang, J.-H. Cheng, W.-N. Su, P. Partovi-Azar, L.-Y. Kuo, M.-C. Tsai, M.-H. Lin, S. Panahian Jand, T.-S. Chan, N.-L. Wu, P. Kaghazchi, H. Dai, P. M. Bieker and B.-J. Hwang, *J. Power Sources*, 2021, **492**, 229508.
40 L. Wang, X. He, J. Li, M. Chen, J. Gao and C. Jiang, *Electrochim. Acta*, 2012, **72**, 114–119.
41 J. Fanous, M. Wegner, M. B. M. Spera and M. R. Buchmeiser, *J. Electrochem. Soc.*, 2013, **160**, A1169–A1170.
42 E. K. Simanjuntak, T. Danner, P. Wang, M. R. Buchmeiser and A. Latz, *Electrochim. Acta*, 2024, **497**, 144571.
43 S. V. Klostermann, J. Kappler, A. Waigum, M. R. Buchmeiser, A. Köhn and J. Kästner, *Phys. Chem. Chem. Phys.*, 2024, **26**, 9998–10007.
44 X. Wang, Y. Qian, L. Wang, H. Yang, H. Li, Y. Zhao and T. Liu, *Adv. Funct. Mater.*, 2019, **29**, 1902929.
45 H. Li, W. Xue, L. Wang and T. Liu, *ACS Appl. Mater. Interfaces*, 2021, **13**, 25002–25009.
46 Y.-Z. Zhang, Z.-Z. Wu, G.-L. Pan, S. Liu and X.-P. Gao, *ACS Appl. Mater. Interfaces*, 2017, **9**, 12436–12444.
47 Y. Z. Zhang, S. Liu, G. C. Li, G. R. Li and X. P. Gao, *J. Mater. Chem. A*, 2014, **2**, 4652–4659.
48 Z. Wen and D. Lu, *J. Electrochem. Soc.*, 2013, **160**, A2311–A2314.
49 H. Peng, X. Wang, Y. Zhao, T. Tan, A. Mentbayeva, Z. Bakenov and Y. Zhang, *J. Nanopart. Res.*, 2017, **19**, 348.
50 H. Liu, Y. Zhang, Y. Li, H. Liu, N. Han and X. Zhang, *ACS Appl. Nano Mater.*, 2023, **6**, 21058–21067.
51 W. Wei, J. Wang, L. Zhou, J. Yang, B. Schumann and Y. NuLi, *Electrochem. Commun.*, 2011, **13**, 399–402.
52 L. Yin, J. Wang, J. Yang and Y. Nuli, *J. Mater. Chem.*, 2011, **21**, 6807.
53 T. Nguyen, C.-K. Yang and Y.-S. Su, *J. Alloys Compd.*, 2025, **1022**, 179886.
54 L. Yin, J. Wang, F. Lin, J. Yang and Y. Nuli, *Energy Environ. Sci.*, 2012, **5**, 6966.
55 J. Li, K. Li, M. Li, D. Gosselink, Y. Zhang and P. Chen, *J. Power Sources*, 2014, **252**, 107–112.
56 T. Nguyen and Y.-S. Su, *Mater. Des.*, 2024, **240**, 112861.
57 K. Kalaiappan, S. Rengapillai, S. Marimuthu, R. Murugan and P. Thiru, *Front. Chem. Sci. Eng.*, 2020, **14**, 976–987.
58 T. Wang, Q. Zhang, J. Zhong, M. Chen, H. Deng, J. Cao, L. Wang, L. Peng, J. Zhu and B. Lu, *Adv. Energy Mater.*, 2021, **11**, 2100448.

© 2025 The Author(s). Published by the Royal Society of Chemistry

Open Access Article. Published on 15 July 2025. Downloaded on 6/21/2026 12:44:31 AM. This article is licensed under a Creative Commons Attribution 3.0 Unported Licence.

59 H. Kim, J.-Y. Hwang, S. Bang, H.-G. Jung and Y.-K. Sun, *J. Mater. Chem. A*, 2022, **10**, 10844–10853.
60 Q. Wu, W. Zhang, S. Li, W. Zhong, H. Zhu, Z. Zeng, C. Yu, S. Cheng and J. Xie, *ACS Appl. Energy Mater.*, 2022, **5**, 5212–5218.
61 X. Huang, J. Liu, Z. Huang, X. Ke, L. Liu, N. Wang, J. Liu, Z. Guo, Y. Yang and Z. Shi, *Electrochim. Acta*, 2020, **333**, 135493.
62 Y. Liu, A. K. Haridas, Y. Lee, K.-K. Cho and J.-H. Ahn, *Appl. Surf. Sci.*, 2019, **472**, 135–142.
63 K. Wang, S. Ju, Q. Gao, G. Xia, G. Wang, H. Yan, L. Dong, Z. Yang and X. Yu, *J. Alloys Compd.*, 2021, **860**, 158445.
64 M. Frey, R. K. Zenn, S. Warneke, K. Müller, A. Hintennach, R. E. Dinnebier and M. R. Buchmeiser, *ACS Energy Lett.*, 2017, **2**, 595–604.
65 H. Liu, R. He, Y. Li, Y. Jin, H. Liu and X. Zhang, *J. Electroanal. Chem.*, 2023, **939**, 117465.
66 A. K. Haridas, J. Heo, Y. Liu, H.-J. Ahn, X. Zhao, Z. Deng, M. Agostini, A. Matic, K.-K. Cho and J.-H. Ahn, *ACS Appl. Mater. Interfaces*, 2019, **11**, 29924–29933.
67 A. Abdul Razzaq, X. Yuan, Y. Chen, J. Hu, Q. Mu, Y. Ma, X. Zhao, L. Miao, J.-H. Ahn, Y. Peng and Z. Deng, *J. Mater. Chem. A*, 2020, **8**, 1298–1306.
68 X. Yuan, B. Zhu, J. Feng, C. Wang, X. Cai and R. Qin, *ACS Appl. Mater. Interfaces*, 2021, **13**, 50936–50947.
69 M. A. Weret, C.-F. J. Kuo, W.-N. Su, T. S. Zeleke, C.-J. Huang, N. A. Sahalie, T. A. Zegeye, Z. T. Wondimkun, F. W. Fenta, B. A. Jote, M.-C. Tsai and B. J. Hwang, *J. Power Sources*, 2022, **541**, 231693.
70 H. Li, W. Xue, W. Xu, L. Wang and T. Liu, *Compos. Commun.*, 2021, **24**, 100675.
71 M. Jiang, K. Wang, S. Gao, R. Wang, J. Han, J. Yan, S. Cheng and K. Jiang, *ChemElectroChem*, 2019, **6**, 1365–1370.
72 R. He, Y. Li, S. Wei, H. Liu, S. Zhang, N. Han, H. Liu, X. Wang and X. Zhang, *J. Alloys Compd.*, 2022, **919**, 165838.
73 X. Chen, L. Peng, L. Wang, J. Yang, Z. Hao, J. Xiang, K. Yuan, Y. Huang, B. Shan, L. Yuan and J. Xie, *Nat. Commun.*, 2019, **10**, 1021.
74 W. Zhang, S. Li, L. Wang, X. Wang and J. Xie, *Sustainable Energy Fuels*, 2020, **4**, 3588–3596.
75 K. Wang, T. Zhao, N. Zhang, T. Feng, L. Li, F. Wu and R. Chen, *Nanoscale*, 2021, **13**, 16690–16695.
76 R. He, Y. Li, Z. Mu, H. Liu, Y. Zhang and X. Zhang, *ACS Appl. Nano Mater.*, 2023, **6**, 23163–23172.
77 J. Wang, L. Yin, H. Jia, H. Yu, Y. He, J. Yang and C. W. Monroe, *ChemSusChem*, 2014, **7**, 563–569.
78 Y. Song, J. Lai, X. Li, J. Huo, C. Zhao and C. He, *Mater. Lett.*, 2021, **296**, 129933.
79 S. M. Sabet, N. Sapkota, S. Chiluwal, T. Zheng, C. M. Clemons, A. M. Rao and S. Pilla, *ACS Sustainable Chem. Eng.*, 2023, **11**, 2314–2323.
80 L. Yin, J. Wang, X. Yu, C. W. Monroe, Y. NuLi and J. Yang, *Chem. Commun.*, 2012, **48**, 7868.
81 S. Ma, Z. Zhang, Y. Wang, Z. Yu, C. Cui, M. He, H. Huo, G. Yin and P. Zuo, *Chem. Eng. J.*, 2021, **418**, 129410.
82 Z.-Q. Xu, R. Zou, W.-W. Liu, G.-L. Liu, Y.-S. Cui, Y.-X. Lei, Y.-W. Zheng, W.-J. Niu, Y.-Z. Wu, B.-N. Gu, M.-J. Liu, F. Ran and Y.-L. Chueh, *Chem. Eng. J.*, 2023, **471**, 144581.
83 A. Abdul Razzaq, G. Chen, X. Zhao, X. Yuan, J. Hu, Z. Li, Y. Chen, J. Xu, R. Shah, J. Zhong, Y. Peng and Z. Deng, *J. Energy Chem.*, 2021, **61**, 170–178.
84 L. Fang, W. Xu, X. Lyu, Y. Liu, B. Reinhart, H. Nguyen and T. Li, *ACS Appl. Energy Mater.*, 2023, **6**, 795–801.
85 J. Lei, J. Chen, A. Naveed, H. Zhang, J. Yang, Y. Nuli and J. Wang, *ACS Appl. Energy Mater.*, 2021, **4**, 5706–5712.
86 Y.-Z. Liang, T.-Y. Hsu and Y.-S. Su, *ACS Appl. Mater. Interfaces*, 2024, acsami.4c03710.
87 Y.-Z. Liang, A. L. Bhat and Y.-S. Su, *ACS Appl. Energy Mater.*, 2024, acsaem.4c02183.
88 C.-W. Huang, T. Nguyen, Y.-C. Chu, J.-K. Chang, P.-Y. Chen and Y.-S. Su, *Int. J. Energy Res.*, 2025, **2025**(1), 4701282.
89 Y. Zhang, Y. Zhao, A. Yermukhambetova, Z. Bakenov and P. Chen, *J. Mater. Chem. A*, 2013, **1**, 295–301.
90 H. Yang, Q. Li, C. Guo, A. Naveed, J. Yang, Y. Nuli and J. Wang, *Chem. Commun.*, 2018, **54**, 4132–4135.
91 Y. Zhang, Z. Wang, Y. Pan, H. Yu, Z. Li, C. Li, S. Wang, Y. Ma, X. Shi, H. Zhang, D. Song and L. Zhang, *Energy Environ. Sci.*, 2024, **17**, 2576–2587.
92 H. Yang, J. Chen, J. Yang, Y. Nuli and J. Wang, *Energy Storage Mater.*, 2020, **31**, 187–194.
93 A. Mayer and M. R. Buchmeiser, *J. Electrochem. Soc.*, 2018, **165**, A3943–A3945.
94 Y. Li, X. Qi, H. Zhou, F. Yang, X. Jin, R. Jiang, Z. Zhu, C. Liang, Z. Li, L. Yuan, L. Qie and Y. Huang, *Angew. Chem., Int. Ed.*, 2025, **64**, e202419995.
95 X. Huang, J. Liu, Z. Huang, X. Ke, L. Liu, N. Wang, J. Liu, Z. Guo, Y. Yang and Z. Shi, *Electrochim. Acta*, 2020, **333**, 135493.
96 K. Wang, T. Zhao, N. Zhang, T. Feng, L. Li, F. Wu and R. Chen, *Nanoscale*, 2021, **13**, 16690–16695.
97 H. M. Kim, J.-Y. Hwang, D. Aurbach and Y.-K. Sun, *J. Phys. Chem. Lett.*, 2017, **8**, 5331–5337.
98 A. Abdul Razzaq, X. Yuan, Y. Chen, J. Hu, Q. Mu, Y. Ma, X. Zhao, L. Miao, J.-H. Ahn, Y. Peng and Z. Deng, *J. Mater. Chem. A*, 2020, **8**, 1298–1306.
99 P. Wang, C. Xia, J. Yang, X. He, K. Lv, S. Ren, H. Song, J. Wang, P. He and H. Zhou, *Sci. Bull.*, 2022, **67**, 256–262.

© 2025 The Author(s). Published by the Royal Society of Chemistry